Print summary page:

Samples returned from the asteroid Ryugu are similar to Ivuna-type carbonaceous meteorites

T. Yokoyama†, K. Nagashima† et al.*

† These authors contributed equally

*Corresponding author H. Yurimoto yuri@ep.sci.hokudai.ac.jp

Introduction: The Hayabusa2 spacecraft made two landings on the asteroid Ryugu in 2019, during which it collected samples of the surface material. Those samples were delivered to Earth in December 2020. The colors, shapes and morphologies of the returned samples are consistent with those observed on Ryugu by Hayabusa2, indicating that they are representative of the asteroid. Laboratory analysis of the samples can determine the chemical composition of Ryugu and provide information on its formation and history.

Rationale: We use laboratory analysis to inform the following the questions: (*i*) what are the elemental abundances of Ryugu?; (*ii*) what are the isotopic compositions of Ryugu?; (*iii*) does Ryugu consist of primary materials produced in the disk from which the Solar System formed, or of secondary materials produced in the asteroid or on a parent asteroid?; (*iv*) when were Ryugu's constituent materials formed?; and (*v*) what (if any) relationship does Ryugu have with meteorites?

Results: We quantified the abundances of 66 elements in Ryugu samples: H, Li, Be, C, O, Na, Mg, Al, Si, P, S, Cl, K, Ca, Sc, Ti, V, Cr, Mn, Fe, Co, Ni, Cu, Zn, Ga, Ge, As, Se, Rb, Sr, Y, Zr, Nb, Mo, Ru, Rh, Pd, Ag, Cd, In, Sn, Te, Cs, Ba, La, Ce, Pr, Nd, Sm, Eu, Gd, Tb, Dy, Ho, Er, Tm, Yb, Lu, Hf, Ta, W, Tl, Pb, Bi, Th, and U. There is a slight variation in chemical compositions between samples from the first and second touchdown sites, but the variations could be due to heterogeneity at the small scale of the samples analyzed.

The Cr-Ti isotopes and abundance of volatile elements are similar to carbonaceous meteorites in the CI (Ivuna-like) chondrite group. The Ryugu samples consist of the minerals magnetite, breunnerite, dolomite, and pyrrhotite as grains embedded in a matrix composed of serpentine and saponite. This is also similar to CI meteorites. Anhydrous silicates are almost absent, indicating extensive liquid water-rock reactions (aqueous alteration) of the material. We conclude that the samples mainly consist of secondary materials formed by aqueous alteration in a parent body, from which Ryugu later formed.

The oxygen isotopes in the bulk Ryugu samples are also similar to those in CI chondrites. We use oxygen isotope thermometry to determine the temperature at which the dolomite and magnetite precipitated from an aqueous solution: 37 ±10 °C. The ^{53}Mn-^{53}Cr isotopes date the aqueous alteration at $5.2^{+0.7}_{-0.8}$ (statistical) $^{+1.6}_{-2.1}$ (systematic) million years after the birth of the Solar System.

Phyllosilicate minerals are the main host of water in the Ryugu samples. The amount of structural water in Ryugu is similar to CI chondrites, but interlayer water is largely absent in Ryugu, suggesting loss of interlayer water to space. The abundance of structural water, and dehydration experiments, indicate the Ryugu samples remained below ~100 °C from the time of aqueous alteration until the present. We ascribe the removal of interlayer water to a combination

of impact heating, solar heating, solar wind irradiation, and long-term exposure to ultra-high vacuum of space. Loss of interlayer water from phyllosilicates could be responsible for the comet-like activity of some carbonaceous asteroids and the ejection of solid material from the surface of asteroid Bennu.

Conclusion: The Ryugu samples are most similar to CI chondrite meteorites, but more chemically pristine than CIs or other Solar System materials that have been analyzed in laboratories. CI chondrites appear to have been modified on Earth or during atmospheric entry. Such modification of CI chondrites could have included the alteration of the structures of organics and phyllosilicates, the adsorption of terrestrial water, and the formation of sulfates and ferrihydrites. Those issues do not affect the Ryugu samples. Those modifications might have changed the albedo, porosity, and density of the CI chondrites, causing the observed differences with Ryugu observed by Hayabusa2, and the Ryugu samples returned to Earth. The Ryugu samples are most closely resembles Solar photosphere in chemical composition among natural samples available in laboratory.

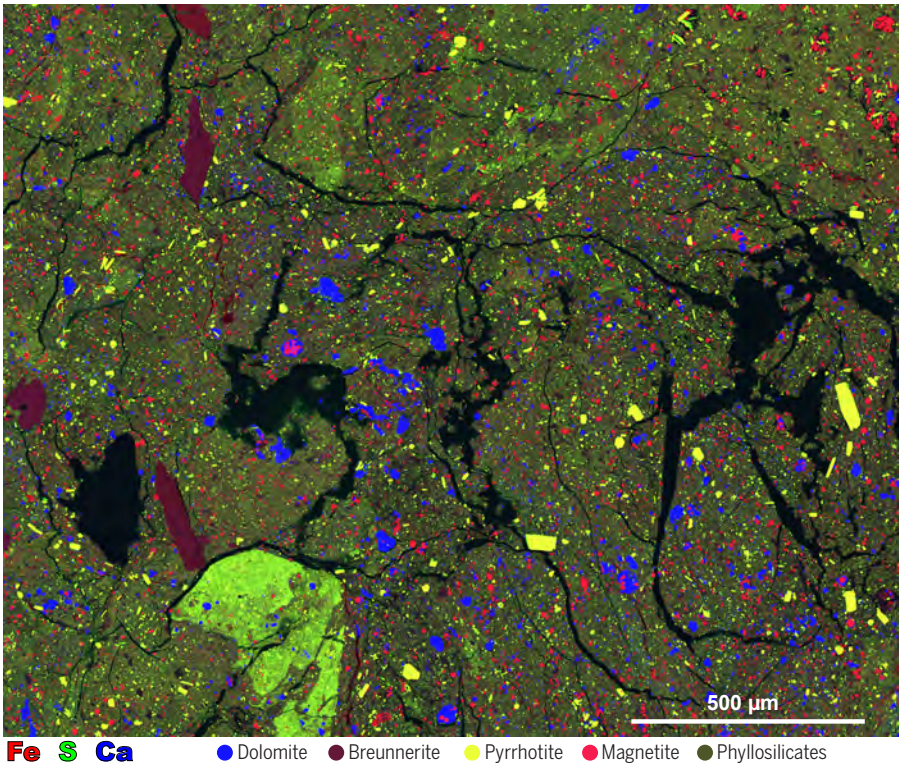

Representative petrography of a Ryugu sample, designated C0002-C1001. Colors indicate elemental abundances determined from X-ray spectroscopy. Lines of iron, sulphur, and calcium are shown as RGB color channels in that order. Combinations of these elements are assigned to specific minerals, as indicated in the legend. All visible minerals were formed by aqueous alteration on Ryugu's parent body.

Samples returned from the asteroid Ryugu are similar to Ivuna-type carbonaceous meteorites

Tetsuya Yokoyama[1]†, Kazuhide Nagashima[2]†, Izumi Nakai[3], Edward D. Young[4], Yoshinari Abe[5], Jérôme Aléon[6], Conel M. O'D. Alexander[7], Sachiko Amari[8], Yuri Amelin[9], Ken-ichi Bajo[10], Martin Bizzarro[11], Audrey Bouvier[12], Richard W. Carlson[7], Marc Chaussidon[13], Byeon-Gak Choi[14], Nicolas Dauphas[15], Andrew M. Davis[15],Tommaso Di Rocco[16], Wataru Fujiya[17], Ryota Fukai[18], Ikshu Gautam[1], Makiko K. Haba[1], Yuki Hibiya[19], Hiroshi Hidaka[20], Hisashi Homma[21], Peter Hoppe[22], Gary R. Huss[2], Kiyohiro Ichida[23], Tsuyoshi Iizuka[24], Trevor R. Ireland[25], Akira Ishikawa[1], Motoo Ito[26], Shoichi Itoh[27], Noriyuki Kawasaki[10], Noriko T. Kita[28], Kouki Kitajima[28], Thorsten Kleine[29], Shintaro Komatani[23], Alexander N. Krot[2], Ming-Chang Liu[4], Yuki Masuda[1], Kevin D. McKeegan[4], Mayu Morita[23], Kazuko Motomura[30], Frédéric Moynier[13], Ann Nguyen[31], Larry Nittler[7], Morihiko Onose[23], Andreas Pack[16], Changkun Park[32], Laurette Piani[33], Liping Qin[34], Sara S. Russell[35], Naoya Sakamoto[36], Maria Schönbächler[37], Lauren Tafla[4], Haolan Tang[4], Kentaro Terada[38], Yasuko Terada[39], Tomohiro Usui[18], Sohei Wada[10], Meenakshi Wadhwa[40], Richard J. Walker[41], Katsuyuki Yamashita[42], Qing-Zhu Yin[43], Shigekazu Yoneda[44], Hiroharu Yui[45], Ai-Cheng Zhang[46], Harold C. Connolly, Jr.[47], Dante S. Lauretta[48], Tomoki Nakamura[49], Hiroshi Naraoka[50], Takaaki Noguchi[27], Ryuji Okazaki[50], Kanako Sakamoto[18], Hikaru Yabuta[51], Masanao Abe[18], Masahiko Arakawa[52], Atsushi Fujii[18], Masahiko Hayakawa[18], Naoyuki Hirata[52], Naru Hirata[53], Rie Honda[54], Chikatoshi Honda[53], Satoshi Hosoda[18], Yu-ichi Iijima[18]‡, Hitoshi Ikeda[18], Masateru Ishiguro[14], Yoshiaki Ishihara[18], Takahiro Iwata[18,55], Kosuke Kawahara[18], Shota Kikuchi[56], Kohei Kitazato[53], Koji Matsumoto[57], Moe Matsuoka[18]§, Tatsuhiro Michikami[58], Yuya Mimasu[18], Akira Miura[18], Tomokatsu Morota[24], Satoru Nakazawa[18], Noriyuki Namiki[57], Hirotomo Noda[57], Rina Noguchi[59], Naoko Ogawa[18], Kazunori Ogawa[18], Tatsuaki Okada[18,60], Chisato Okamoto[52]‡, Go Ono[18], Masanobu Ozaki[18,55], Takanao Saiki[18], Naoya Sakatani[61], Hirotaka Sawada[18], Hiroki Senshu[56], Yuri Shimaki[18], Kei Shirai[18], Seiji Sugita[24], Yuto Takei[18], Hiroshi Takeuchi[18], Satoshi Tanaka[18], Eri Tatsumi[62], Fuyuto Terui[63], Yuichi Tsuda[18], Ryudo Tsukizaki[18], Koji Wada[56], Sei-ichiro Watanabe[20], Manabu Yamada[56], Tetsuya Yamada[18], Yukio Yamamoto[18], Hajime Yano[18], Yasuhiro Yokota[18], Keisuke Yoshihara[18], Makoto Yoshikawa[18], Kent Yoshikawa[18], Shizuho Furuya[18], Kentaro Hatakeda[64], Tasuku Hayashi[18], Yuya Hitomi[64], Kazuya Kumagai[64], Akiko Miyazaki[18], Aiko Nakato[18], Masahiro Nishimura[18], Hiromichi Soejima[64], Ayako Suzuki[64], Toru Yada[18], Daiki Yamamoto[18], Kasumi Yogata[18], Miwa Yoshitake[18], Shogo Tachibana[65], Hisayoshi Yurimoto[10,36]*

Affiliations:

[1]Department of Earth and Planetary Sciences, Tokyo Institute of Technology; Tokyo 152-8551, Japan.

[2]Hawai‘i Institute of Geophysics and Planetology, University of Hawai‘i at Mānoa; Honolulu, HI 96822, USA.

[3]Department of Applied Chemistry, Tokyo University of Science; Tokyo 162-8601, Japan.

[4]Department of Earth, Planetary, and Space Sciences, University of California, Los Angeles; Los Angeles, CA 90095, USA.

[5]Graduate School of Engineering Materials Science and Engineering, Tokyo Denki University; Tokyo 120-8551, Japan.

[6]Institut de Minéralogie, de Physique des Matériaux et de Cosmochimie, Sorbonne Université, Museum National d'Histoire Naturelle, Centre National de la Recherche Scientifique Unité Mixte de Recherche 7590, Institut de recherche pour le développement; 75005 Paris, France.

[7]Earth and Planets Laboratory, Carnegie Institution for Science; Washington, DC, 20015, USA.

[8]McDonnell Center for the Space Sciences and Physics Department, Washington University; St. Louis, MO 63130, USA.

[9]Guangzhou Institute of Geochemistry, Chinese Academy of Sciences; Guangzhou, GD 510640, China.

[10]Department of Natural History Sciences, Hokkaido University; Sapporo 001-0021, Japan.

[11]Centre for Star and Planet Formation, Globe Institute, University of Copenhagen; Copenhagen, K 1350, Denmark.

[12]Bayerisches Geoinstitut, Universität Bayreuth; Bayreuth 95447, Germany.

[13]Université de Paris, Institut de physique du globe de Paris, Centre National de la Recherche Scientifique; 75005 Paris, France

[14]Department of Physics and Astronomy, Seoul National University; Seoul 08826, Republic of Korea.

[15]Department of the Geophysical Sciences and Enrico Fermi Institute, The University of Chicago; Chicago, IL 60637, USA.

[16]Faculty of Geosciences and Geography, University of Göttingen; Göttingen, D-37077, Germany.

[17]Faculty of Science, Ibaraki University; Mito 310-8512, Japan.

[18]Institute of Space and Astronautical Science / Jaxa Space Exploration Center, Japan Aerospace Exploration Agency; Sagamihara 252-5210, Japan.

[19]Department of General Systems Studies, The University of Tokyo; Tokyo 153-0041, Japan.

[20]Department of Earth and Planetary Sciences, Nagoya University; Nagoya 464-8601, Japan.

[21]Osaka Application Laboratory, Rigaku Corporation; Osaka 569-1146, Japan.

[22]Max Planck Institute for Chemistry; Mainz 55128, Germany.

[23]Analytical Technology Division, Horiba Techno Service Co., Ltd.; Kyoto 601-8125, Japan.

[24]Department of Earth and Planetary Science, The University of Tokyo; Tokyo 113-0033, Japan.

[25]School of Earth and Environmental Sciences, The University of Queensland; St Lucia QLD 4072, Australia.

[26]Kochi Institute for Core Sample Research, Japan Agency for Marine-Earth Science and Technology; Kochi 783-8502, Japan.

[27]Department of Earth and Planetary Sciences, Kyoto University; Kyoto 606-8502, Japan.

[28]Department of Geoscience, University of Wisconsin- Madison; Madison, WI 53706, USA.

[29]Max Planck Institute for Solar System Research; 37077 Göttingen, Germany.

[30]Thermal Analysis Division, Rigaku Corporation; Tokyo 196-8666, Japan.

[31]Astromaterials Research and Exploration Science Division, National Aeronautics and Space Administration Johnson Space Center; Houston, TX 77058, USA.

[32]Division of Earth-System Sciences, Korea Polar Research Institute; Incheon 21990, Korea.

[33]Centre de Recherches Pétrographiques et Géochimiques, Centre National de la Recherche Scientifique - Université de Lorraine; 54500 Nancy, France.

[34]School of Earth and Space Sciences, University of Science and Technology of China; Anhui 230026, China.

[35]Department of Earth Sciences, Natural History Museum; London, SW7 5BD, UK.

[36]Isotope Imaging Laboratory, Hokkaido University; Sapporo 001-0021, Japan.

[37]Institute for Geochemistry and Petrology, Department of Earth Sciences, ETH Zurich, Zurich, Switzerland.

[38]Department of Earth and Space Science, Osaka University; Osaka 560-0043, Japan.

[39]Spectroscopy and Imaging Division, Japan Synchrotron Radiation Research Institute; Hyogo 679-5198 Japan.

[40]School of Earth and Space Exploration, Arizona State University; Tempe, AZ 85281, USA.

[41]Geology, University of Maryland, College Park, MD 20742, USA.

[42]Graduate School of Natural Science and Technology, Okayama University; Okayama 700-8530, Japan.

[43]Department of Earth and Planetary Sciences, University of California; Davis, CA 95616, USA.

[44]Department of Science and Engineering, National Museum of Nature and Science; Tsukuba 305-0005, Japan.

[45]Department of Chemistry, Tokyo University of Science; Tokyo 162-8601, Japan.

[46]School of Earth Sciences and Engineering, Nanjing University; Nanjing 210023, China.

[47]Department of Geology, School of Earth and Environment, Rowan University; Glassboro, NJ 08028, USA.

[48]Lunar and Planetary Laboratory, University of Arizona; Tucson, AZ 85705, USA.

[49]Department of Earth Science, Tohoku University; Sendai, 980-8578, Japan.

[50]Department of Earth and Planetary Sciences, Kyushu University; Fukuoka 819-0395, Japan.

[51]Earth and Planetary Systems Science Program, Hiroshima University; Higashi-Hiroshima, 739-8526, Japan.

[52]Graduate School of Science, Kobe University; Kobe 657-8501, Japan.

[53]Department of Computer Science and Engineering, University of Aizu; Aizu-Wakamatsu 965-8580, Japan.

[54]Faculty of Science and Technology, Kochi University; Kochi 780-8520, Japan.

[55]The Graduate University for Advanced Studies, Sokendai, Kanagawa 240-0193, Japan

[56]Planetary Exploration Research Center, Chiba Institute of Technology; Narashino 275-0016, Japan.

[57]National Astronomical Observatory of Japan; Mitaka 181-8588, Japan.

[58]Faculty of Engineering, Kinki University; Higashi-Hiroshima 739-2116, Japan.

[59]Academic Assembly Institute of Science and Technology, Niigata University; Niigata 950-2181, Japan.

[60]Department of Chemistry, The University of Tokyo; Tokyo 113-0033, Japan.

[61]College of Science Department of Physics, Rikkyo University; Tokyo 171-8501, Japan.

[62]Instituto de Astrofísica de Canarias, University of La Laguna; Tenerife, Spain.

[63]Graduate School of Engineering, Kanagawa Institute of Technology; Atsugi 243-0292, Japan.

[64]Marine Works Japan Ltd.; Yokosuka 237-0063 Japan.

[65]UTokyo Organization for Planetary and Space Science, University of Tokyo; Tokyo 113-0033, Japan.

*Corresponding author. Email: yuri@ep.sci.hokudai.ac.jp

†These authors contributed equally to this work.

‡Deceased.

§Present address. Laboratoire d'études spatiales et d'instrumentation en astrophysique, Observatoire de Paris; 92195 Meudon, France.

Abstract:

Carbonaceous meteorites are thought to be fragments of C-type (carbonaceous) group of asteroids. We measure mineralogy, bulk chemical and isotopic compositions in samples of a C-type group asteroid (162173) Ryugu retrieved by the Hayabusa2 spacecraft. We find that Ryugu is mainly composed of materials similar to carbonaceous chondrite meteorites, particularly the CI (Ivuna-like) group. The samples consist predominantly of minerals formed in aqueous fluid in a parent planetesimal. The fluid altered primary minerals at $5.2^{+0.7}_{-0.8}$ (Stat.) $^{+1.6}_{-2.1}$ (Syst.) million years after formation of the first solids in the Solar System, at the temperature of 37±10°C. After aqueous alteration, the Ryugu samples were likely never heated above ~100°C. The Ryugu samples are most closely resembles Solar photosphere in chemical composition among natural samples available in laboratory.

One-Sentence Summary:

Returned samples from C-type asteroid Ryugu show strong similarities to CI (Ivuna-like) carbonaceous chondrites.

(112 characters; <125 characters and spaces)

Main Text:

Meteorites are fragments of asteroids, but identifications of the specific parent asteroid are rarely available. Samples of asteroid (25143) Itokawa returned by the Hayabusa mission showed that S-type (stony by a remote sensing classification) asteroids are composed of materials consistent with the ordinary chondrite meteorites (*1, 2*). The Hayabusa2 (*3*) spacecraft was launched on 2014 December 3 to collect samples of the near-Earth Cb-type (a type of C (carbonaceous) complex by a remote sensing classification) asteroid (162173) Ryugu, with the goal of determining the relationship between C-type (carbonaceous by a remote sensing classification) asteroids and the carbonaceous chondrite meteorites. Observations of Ryugu from Hayabusa2 after rendezvous showed that: (*i*) Ryugu is darker than every meteorite group (*4, 5*); (*ii*) Ryugu contains ubiquitous phyllosilicate minerals (*4, 6*); (*iii*) Ryugu's surface experienced heating above 300 °C (*6*); and (*iv*) Ryugu materials are probably more porous than carbonaceous chondrites (*7, 8*). These results indicated that carbonaceous chondrites are plausible analogs of Ryugu, but do not completely match the spacecraft observations. Laboratory analysis of the samples of Ryugu returned by Hayabusa2 are required to determine why.

During 2019, the Hayabusa2 spacecraft made two landings on Ryugu to collect materials (*9*) and delivered the collected samples to Earth on 2020 December 6. The returned samples are rock fragments ranging in size up to ~10 mm, with a total mass of 5.4 grams. Their colors, shapes, and morphologies are consistent with those observed on the surface by Hayabusa2, indicating that the returned samples are representative of Ryugu's surface (*10, 11*). The samples were recovered in a non-destructive manner and examined under contamination-controlled conditions at the JAXA Extraterrestrial Sample Curation Center before delivery to the initial analysis teams in June 2021 (*10*). Our team was allocated ~125 mg of samples, containing both powder and particles from the first and the second touchdown sites (*12*). We used ~95 mg for this paper.

Petrology and mineralogy

We prepared polished sections from particle samples from the first touchdown site （A0058) and from the second touchdown site (C0002) (*12*). The prtrography and mineralogy as well as chemical compositions minerals are determined by electron microscopy (*12*).

The Ryugu samples are mixtures of mechanical fragments composed of fine-grained materials of phyllosilicate minerals, predominantly serpentine and saponite - and coarser grains dominated by carbonates, magnetite, and sulfides (Figs. 1A, B, and D). No Ca-Al-rich inclusions (CAIs) or chondrules, characteristic constituents of most chondrite meteorites were evident in the allocated samples. The serpentine:saponite molar ratio is approximately 3:2, based on the chemical compositions of the phyllosilicate minerals (Fig. 1C). The coarser-grained minerals in the polished sections are dolomite ($CaMg(CO_3)_2$), breunnerite ($(Mg, Fe, Mn)CO_3$), pyrrhotite ($Fe_{1-x}S$; x=0 to 0.17), and magnetite (Fe_3O_4)(Fig. 1B). These are distributed throughout the sections (Fig. 1D), and in small vein (Fig. 1A). Calcite ($CaCO_3$), pentlandite ($(Fe,Ni)_9S_8$), cubanite ($CuFe_2S_3$), ilmenite ($FeTiO_3$), apatite ($(Ca_5(PO_4)_3(OH,F,Cl)$), and Mg-Na-phosphate are present as accessory minerals. Anhydrous silicates, such as olivine and pyroxene, are common in chondrites, but are very rare in Ryugu samples, occurring only as discrete grains smaller than ~10 μm across. No metal grains were identified. Overall, the petrology and mineralogy of the Ryugu samples most closely resembles the CI (Ivuna-like) group of chondrite meteorites, which have experienced extensive aqueous alteration (*13*). However, sulfates and ferrihydrite, which are commonly observed in CI chondrites, were not identified in the Ryugu samples we studied.

Bulk chemical and isotopic compositions

Bulk chemical compositions of small grain aggregate samples for the first touchdown site（A0106 and A0107) and the second touchdown site (C0108) were determined using ~25 mg samples for each site (*12*). X-ray fluorescence (XRF) analysis and inductively coupled plasma mass spectrometry (ICP-MS) are applied. The same samples, ICP-MS analysis, and thermal ionization mass spectrometry (TIMS) analysis were used for titanium and chromium isotope analyses after the chemical analyses.

We found no systematic differences in chemical composition between the samples from the first and second touchdown sites (Fig. 2). We did find variations in bulk composition within each of those sample, which are most likely due to heterogeneity at small scales (see Supplementary Text). The masses of the samples analyzed were less than 30 mg; coarser-grained water-precipitated minerals might not be uniformly distributed at that scale (a cross-section of ~10 mg block is shown in Fig. 1D).Spatial heterogeneity in the mineral distributions is observed for carbonates (dolomite) and sulfides (pyrrhotite), which both precipitate from aqueous solution during alteration in the parent planetesimal of Ryugu (Fig. 1). We find different concentrations of rare earth elements (REEs) between samples from the first touchdown site and the second touchdown site (*12*), with both being higher than the REE abundance in CI chondrites (Fig. 2). These variable enrichments could be due to depletion of H_2O, relative to CI chondrites (see below), and the heterogeneous distribution of REE-rich Ca-phosphate grains (*14, 15*). Heterogeneity at similar scales has been observed in CI chondrites (*16, 17*) and in the ungrouped carbonaceous chondrite Tagish Lake (*18*).

We do not observe systematic depletions of elemental abundances, relative to CI chondrites, with decreasing 50% condensation temperature of element (volatility) (Fig. 2). This is unlike other groups of carbonaceous chondrites, which show various degrees of depletion with volatility (*19*). The high abundance of moderately and highly volatile elements in the Ryugu samples indicates that Ryugu is composed of materials that are related to the CI chondrite group. However, the elemental abundances of hydrogen and oxygen are highly depleted in the Ryugu samples compared to CI chondrites, which we interpret as removal of H_2O.

Previous studies have found a dichotomy in the isotopic compositions of titanium and chromium between non-carbonaceous (NC)-like and carbonaceous (CC)-like isotope ratios (*20, 21, 22, 23*). The bulk titanium and chromium isotopic ratios for the Ryugu samples are similar to the CB (Bencubbin-like) and CI chondrite values (see Supplementary Text), which are both CCs (Fig. 3). CB chondrites are metal rich (*24*), unlike the Ryugu samples, so are unlikely to be directly related.

Oxygen isotopic composition

Bulk oxygen isotopic compositions of the Ryugu samples from the first (~4 mg of aggregate sample: A0107) and the second (~1 mg of fragment from particle sample: C0002) touchdown sites were determined by laser-fluorination isotope-ratio mass-spectrometry (LF-IRMS) (*12*). Oxygen isotopic compositions of secondary minerals from the first touchdown site were determined by secondary ion mass spectrometry (SIMS) using the polished section used for petrology and mineralogy (*12*).

Oxygen isotopes measured in the bulk Ryugu samples overlap with those of the bulk samples of the Orgueil CI chondrite (Fig. 4). We interpret the variation in $\delta^{18}O$; defined as the permil deviation from the $^{18}O/^{16}O$ ratio of standard-mean-ocean-water, as due to the

heterogeneous distributions of the constituent minerals, which may have very different isotopic compositions, including phyllosilicates, carbonates, and magnetite. Two ~2-mg Ryugu samples from the first touchdown site have consistent $\Delta^{17}O$ values (defined as the permil deviation from the terrestrial fractionation line) (*12*) with an average $\Delta^{17}O = 0.68 \pm 0.05$ ‰ (uncertainty of 2 standard deviations (SD)). These are higher $\Delta^{17}O$ values than three samples of Orgueil analyzed in the same session, which have $\Delta^{17}O = 0.42 – 0.53$ ‰). Another Ryugu sample from the second touchdown site analyzed in a different laboratory has a lower value of $\Delta^{17}O = 0.44 \pm 0.05$ ‰, which is consistent with values for Orgueil analyzed with the same equipment ($\Delta^{17}O = 0.39 – 0.57$ ‰). We therefore ascribe the differences between the Ryugu samples as due to heterogeneity on small scales or different sampling sites on Ryugu, not systematic differences between the laboratories. The average $\Delta^{17}O$ value of the three Ryugu samples, 0.61 ±0.28 (2SD), is slightly higher than the average for the Orgueil samples of 0.48 ±0.15 (2SD, n=5; n: numbers of sampling values), a single measurement of the CI chondrite Ivuna, with 0.41 ±0.05 ‰, and prior measurements of CI chondrites (0.39 – 0.47 ‰, (*25*)). The difference may reflect either original heterogeneity between small samples, or result from contamination of the meteorite samples by terrestrial water incorporated by the phyllosilicates, sulfates, iron oxides and iron hydroxides. The discrepancy in the $\Delta^{17}O$ values between Ryugu and Orgueil (~0.15 ‰ offset) persists despite heating both groups of samples to ~116 °C for 2–4 hours to remove adsorbed water, indicating that any terrestrial contamination in the Orgueil samples is part of the structure of the minerals, not adsorbed to surfaces.

Dolomite grains in the Ryugu samples are enriched in ^{18}O relative to the whole rock values, but have $\Delta^{17}O$ values consistent with the whole rock (Fig. 4). The constituent minerals are generally consistent with mass-dependent fractionation. The oxygen isotope ratios of dolomite in Ryugu overlap with those of dolomite from Ivuna (Fig. 4). Ryugu magnetite is depleted in ^{18}O, relative to the whole rock value, with all but one measurement being consistent with mass fractionation. The oxygen isotope ratios of Ryugu magnetite grains are consistent with those of Ivuna (*26, 27*). The distributions of $^{18}O/^{16}O$ ratios and the consistency of $\Delta^{17}O$ values indicate isotopic equilibrium during growth of the minerals produced by aqueous alteration.

In one polished section, dolomite and magnetite grains are located within ~100 μm of each another (Fig. S1). The dolomite $\Delta^{17}O$ value is –0.7 ±0.9 ‰ (2SD) (*12*), while the magnetite grains have consistent $\Delta^{17}O$ values, with a mean of –0.1 ±0.4 ‰ (2 standard error (SE)). Because the $\Delta^{17}O$ values of dolomite and magnetite grains are within their mutual uncertainties, they may have precipitated from the same fluid. Assuming isotopic equilibrium, we use oxygen-isotope thermometry (*28-31*) to estimate the temperature at which the dolomite-magnetite pair precipitated. The $\delta^{18}O$ values of the dolomite and magnetite are 29.9 ±0.9 ‰ (2SD) and –3.0 ±1.1 ‰ (2SD), respectively. The difference in $\delta^{18}O$ values between the dolomite and magnetite is 32.9 ±1.4 ‰, corresponding to an equilibration temperature of 37 ±10 °C (Fig. S2). The temperature is in the range (10 – 150 °C) of previous estimates for aqueous alteration of CI chondrites (*25, 32–34*). We also estimate (*12*) the oxygen isotope ratios of the water and serpentine that would have been in equilibrium with magnetite and dolomite grains, finding ($\delta^{18}O$, $\delta^{17}O$) = (1.0 ±1.0 ‰, 0.3 ±1.0 ‰) for the water and (18.6 ±2.0 ‰, 9.2 ±1.0 ‰) for serpentine (Figs. 4 and S2). The value for serpentine is consistent with that of the whole rock, as we expected due to the high abundance of serpentine in the samples. These measurements indicate that oxygen-isotopes were in equilibrium, or close to it, during aqueous alteration of the Ryugu samples.

^{53}Mn-^{53}Cr dating

The precipitation of dolomite and magnetite during aqueous alteration can be dated using the ^{53}Mn-^{53}Cr system (*12*), which is based on the decay of the short-lived radionuclide ^{53}Mn to ^{53}Cr (half-life: 3.7 Myr). The ^{53}Mn-^{53}Cr system for dolomite in the Ryugu and Ivuna samples were measured by SIMS using the polished section used for petrology and mineralogy (*12*) and are shown in Figure 5.

The slopes of plots correspond with initial ^{53}Mn/^{55}Mn ratios of (2.55 ±0.35) ×10^{-6} (2SD) for Ryugu and (3.14 ±0.28) ×10^{-6} (2SD) for Ivuna (see Supplementary Text). Both initial values are consistent with those of CI dolomites obtained in previous studies (*35, 36*). We compare the initial ^{53}Mn/^{55}Mn ratio to that of the D'Orbigny meteorite (*37*), an angrite which has been precisely dated and can be compared to ages of the oldest CAIs from CV (Vigarano-type) chondrites (*38-40*). We find that dolomite precipitation in the Ryugu sample occurred at $5.2^{+0.7}_{-0.8}$ million years after the oldest CAI formation, conventionally used to represent the formation of the Solar System. However, there is additional systematic uncertainty in this dolomite precipitation date because the initial Solar System ratio of ^{53}Mn/^{55}Mn is not precisely constrained. If we adopt different initial ^{53}Mn/^{55}Mn ratios than found for D'Orbigny, the dolomite precipitation date changes to 4.8 million years (*41*) or 6.8 million years (*42*) after the CAI formation. There may be additional systematic uncertainty in the ^{53}Mn-^{53}Cr age due to inherent analytical limitations of the measurement technique (*12*). Then the precipitation date may change to 3.1 to 6.8 million years after the CAI formation.

H_2O and CO_2 sources

Gas release curves from Ryugu samples (particle samples of A0040 and A0094) of the first touchdown site and Ivuna sample were measured with increasing heating temperature by thermogravimetric analysis coupled with mass spectrometry (TG-MS) and combination analyses of pyrolysis and combustion (EMIA-Step) (*12*). Mass decrease of the samples during heating (mass loss) was also measured simaltaneously.

The mass loss curve and differential of mass loss (DTG) curve (*12*) for our Ryugu and Ivuna samples are shown in Figure 6 (see Supplementary Text). The results for Ivuna are similar to previous results (*43*). For Ryugu, we find a total mass loss of 15.38±0.50 wt.%, which is ~30% smaller than that of Ivuna (Data S6). The species responsible for the mass loss are mainly H_2O and CO_2 for both Ivuna and Ryugu (Fig. 6). SO_2 might also be substantial, but we were unable to quantify it due to lack of an appropriate standard (*12*).

The total weight fractions of H_2O and CO_2 gases released from the Ryugu sample measured using mass spectrometry coupled with thermogravimetric analysis (TG-MS), are larger (20.78±1.40 wt.%) than the real total mass loss (15.38±0.50 wt.%) measured using TG alone (*12*), we interpret this as indicating that carbonates were not the only sources of CO_2 during the TG-MS measurement, with organic carbon being oxidized to CO_2 by residual O_2 in the He gas flow used for the experiment, producing a spurious excess of CO_2 in the mass spectrometry. Because decomposition of carbonates occurs within a small temperature range (*43*), we are confident that the sharp CO_2 peaks at 600–800 °C (Fig. 6) are due to carbonates. We observed two carbonates peaks for the Ryugu samples, which the petrographic results above showed contain three types of carbonate (dolomite, breunnerite, and calcite). We were unable to attribute specific peaks to specific carbonates. The double peaks might arise from sealed pore spaces, because we analyzed intact chips, not powders.

The remaining broad continuum peak is probably due to oxidation of organic carbon by the indigenous oxygen in organics in the sample and by residual O_2 in the He gas flow of the instrument. Therefore, we assign the CO_2 peak to carbonates and the reminder to organics, as shown in Figure 6. The organic carbon contents are lower limits because the TG-MS leaves some organic carbon in the sample. The organic carbon and total carbon concentrations we found using the TG-MS were lower than those measured using the combination analyses of pyrolysis and combustion (EMIA-Step) (*12*) (Data S6). We estimate that 74±3% of Ryugu organic carbon was released in TG-MS as the broad organic carbon continuum, and 93±4% for Ivuna. The profiles of the broad organic carbon continuum are different for both samples, indicating differing organic components in Ryugu and Ivuna.

Many peaks are apparent in the H_2O release curves (Fig. 6). We identify adsorbed H_2O from sulfates released at ~250 °C, and a larger amount of H_2O from phyllosilicates at ~600 °C. Because the phyllosilicates consist of serpentine and saponite (Fig. 1C), serpentine contains structural OH sites in the crystal structure, while saponite contains interlayer H_2O in addition to structural OH sites. The petrologic and mineralogic observations suggest that the sulfate contribution is negligible for Ryugu, but not for Ivuna. The SO_2 and H_2O peak releases coincide in Ivuna (at both 250 °C and 450 °C), but not Ryugu. We conclude that phyllosilicates are the dominant source of H_2O released from the Ryugu sample.

Dehydration of the interlayer H_2O of saponite is complete at 170 °C (peaking at 90 °C) for Ryugu and complete at 350 °C (peaking at 100 °C) for Ivuna. Dehydroxylation of structural OH in saponite and serpentine occurs at 300 – 800 °C for Ryugu and at 350–800 °C for Ivuna. The structural OH is dominant (6.54±0.32 wt.% H_2O) in the Ryugu sample, with smaller amounts of interlayer H_2O (0.30±0.01 wt.% H_2O). Both forms of H_2O are present at similar levels in Ivuna (Data S6).

Inorganic/organic correlations for hydrogen/carbon

We performed an EMIA-Step analyses of the Ryugu and Ivuna samples (*12*). This showed the total carbon concentration in Ivuna is 3.31±0.33 wt.% (see Supplementary Text), of which 90 % is organic carbon (Fig. 7, Data S6), values which are consistent with prevuous results of (*44*). The total hydrogen in Ivuna is 1.59±0.08 wt.%, of which 89 % is inorganic hydrogen, which is also consistent with previous results (*44*). The total H_2O for Ivuna is 12.73±0.63 wt.%, distributed as 6.58±0.32 wt.% interlayer H_2O and 6.15±0.30 wt.% as structural-OH or H_2O in the phyllosilicates.

Ryugu contains less H_2O than Ivuna. The total H_2O is 6.84±0.34 wt.% including 0.30±0.01 wt.% interlayer H_2O and 6.54±0.32 wt.% structural-OH or H_2O (Data S6). The latter value is similar to Ivuna. The total hydrogen is 0.94±0.05 wt.% for Ryugu, and the inorganic hydrogen (i.e., H_2O) comprises 81 % of the total hydrogen. The amount of organic carbon in Ryugu is 3.08±0.30 wt.%, indistinguishable from that in Ivuna (2.97±0.29 wt.%) (Fig. 7, Data S6). This implies that inorganic/organic matter ratio is similar in the Ryugu and the Ivuna samples studied. This rules out the possibility that Ryugu's low albedo is due to higher organic carbon contents than CI chondrites (*45*). However, the total carbon is higher in Ryugu (4.63±0.23 wt.%) than in Ivuna, due to the higher abundances of carbonates in the Ryugu samples.

Formation history of Ryugu

As mentioned above, aqueous alteration occurred in the Ryugu parent body because aqueous fluid is not stable in the asteroid Ryugu. The CI-like elemental abundances of Ryugu suggest that its parent body accreted all elements of the Solar System with 50 % condensation temperatures higher than 500 K, along with ice-forming elements (Fig. 2). Ryugu's parent body was probably closely related to the parent body(ies) of the CI chondrites. We assume that the accreted material was mainly anhydrous dust and ice. Physical modeling of the thermal evolution of a water ice-bearing CI-like planetesimal (*35*), and our oxygen-isotope thermometry suggests that the Ryugu material accreted 2–4 million years after the birth of the Solar System. Approximately one to two million years later, or roughly 5 million years after the birth of the Solar System (Fig. 5), the Ryugu material experienced aqueous alteration resulting in precipitation of dolomite and magnetite from an aqueous solution at about 37 °C.

The aqueous alteration of the primary accreted Ryugu materials was very extensive. The saponite produced by this fluid-assisted alteration in the parent body of Ryugu must have contained large amounts of interlayer water (~7 wt.%) in its crystal structure when it formed under saturated water activity, as observed in Ivuna (Data S6). The low abundance of interlayer water in the Ryugu samples (0.3 wt.%) indicates that it later escaped to space, most likely after disruption of the parent body and formation of the rubble pile asteroid Ryugu. We cannot definitively identify the dehydration mechanism, but suggest it may have included some combination of impact heating, solar heating, space weathering, and long-term exposure of the asteroid surface to the ultra-high vacuum of space. An estimate of the dehydration temperature would be 170 °C because interlayer water of Ryugu dehydrates completely at 170 °C as mentioned above. The dehydration speed of the interlayer water is as that 20 % of total interlayer water is escaped per minute around the peak temperature of 90 °C (Data S7) (*12*). Moreover, ambient space pressure in Ryugu, which is much lower than the experimental pressure of 10^5 Pa, would accelerate the dehydration speed. Such high dehydration speed gives enough time to complete dehydration of the interlayer water for geological events that occurred in Ryugu. Therefore, it is possible that after aqueous alteration the Ryugu samples have never been heated above ~100 °C because a small peak of interlayer water is still emitted at 90 °C (Fig. 6). These temperatures rule out the previously proposed thermal history of Ryugu (*6*), which was based on laboratory heating experiments of carbonaceous chondrites. The temperatures we estimate are consist with Hayabusa2 observations of the surface temperature at the present orbit of Ryugu (*7*).

Some asteroids show comet-like activity, the origin of which is uncertain and might involve several mechanisms (*46*). This activity can be subtle, as in the B-type (bluish and spectroscopically similar to C-type) asteroid Bennu, where ejections of dust particles and rocks have been observed (*47*). Thermal fracturing, phyllosilicate dehydration, and meteoroid impact were proposed (*47*) as explanations for the ejection of solid particles from Bennu's surface. Our finding that saponite in Ryugu is partially dehydrated supports the possibility that volatile release from phyllosilicates can induce comet-like activity at the surface of low-perihelion carbonaceous asteroids. Possible mechanisms to lift dust and rocks from asteroidal surfaces may be (*i*) anisotropic release of water molecules from phyllosilicate-rich dust particles, imparting a net momentum to those particles, and (*ii*) buildup of vapor pressure in sealed pore space, leading to the pore bursting and propelling dust particles away from the surface. Phyllosilicate dehydration could also play a role in the production of interplanetary dust particles and micrometeorites. The thermal release pattern of Ivuna (Fig. 6) shows that interlayer water is lost from saponite at a temperature of ~0 to 200 °C. The maximum surface temperatures of ~100 °C for Ryugu (*7*) and ~170 °C for Bennu (*48*) would therefore be sufficient for such devolatilization to take place. If

so, the devolatilization is largely complete for surface particles on Ryugu, as particle ejections from the asteroid surface were not observed by the Hayabusa2 spacecraft.

Implications for CI chondrites and cosmochemistry

The CI chondrites are the meteorites whose elemental compositions most closely matches measurements of the solar photosphere (*49*) except for noble gases, hydrogen, carbon, nitrogen, oxygen and lithium. CI chondrites experienced pervasive aqueous alteration, during water-rock interactions in the early Solar System. Less than a dozen CI chondrites are known and have all been on Earth for decades to centuries (the most recent fall was 1965). It is therefore unknown how far handling and exposure to atmospheric moisture has modified their mineralogies and elemental compositions. Unlike CI chondrites, the Ryugu samples are nearly free of sulfates, ferrihydrite, and interlayer water. This could be due to either CI chondrites having originated on parent asteroids with higher water contents than Ryugu, or having been contaminated by terrestrial moisture during residence on Earth (*50, 51*). The lower abundance of anhydrous silicates and the small but measurable offset in $\Delta^{17}O$ between Ryugu and the Orgueil CI chondrite (Fig. 4) support the terrestrial contamination explanation. The slightly higher $\Delta^{17}O$ values of Orgueil in this study compared to earlier studies could be explained if O-isotope exchange in structural-OH water of CI chondrites happened under room temperature conditions. The gas emission patterns measured in the TG-MS and EMIA-Step analyses of Ryugu differ from those of the Ivuna CI chondrite (Figs. 6 and 7). This suggests that the structures of the organic matter differ between Ryugu samples and Ivuna, possibly due to modification during residence on Earth.

We conclude that the Ryugu samples are more chemically pristine that other Solar System materials analyzed in laboratories (including CI meteorites). The materials observed in CI chondrites may have been modified on Earth, so no longer reflect their states in space. Possible causes are phyllosilicate hydration, organic matter transformation and contamination, adsorption or reaction of atmospheric components, and oxidation. These modifications might have changed the albedo, porosity, and density of the CI chondrites, causing the observed differences with Ryugu observed by Hayabusa2 (*5, 7*), and the Ryugu samples returned to Earth (*10*).

References and Notes

1. H. Yurimoto *et al.*, Oxygen isotopic compositions of asteroidal materials returned from Itokawa by the Hayabusa mission. *Science* **333**, 1116-1119 (2011).
2. T. Nakamura *et al.*, Itokawa dust particles: A direct link between S-type asteroids and ordinary chondrites. *Science* **333**, 1113-1116 (2011).
3. S. Tachibana *et al.*, Hayabusa2: Scientific importance of samples returned from C-type near-Earth asteroid (162173) 1999 JU_3. *Geochem. J.* **48**, 571-587 (2014).
4. K. Kitazato *et al.*, The surface composition of asteroid 162173 Ryugu from Hayabusa2 near-infrared spectroscopy. *Science* **364**, 272-275 (2019).
5. S. Sugita *et al.*, The geomorphology, color, and thermal properties of Ryugu: Implications for parent-body processes. *Science* **364**, eaaw0422 (2019).
6. K. Kitazato *et al.*, Thermally altered subsurface material of asteroid (162173) Ryugu. *Nature Astronomy* **5**, 246-250 (2021).
7. T. Okada *et al.*, Highly porous nature of a primitive asteroid revealed by thermal imaging. *Nature* **579**, 518-522 (2020).

8. M. Grott *et al.*, Low thermal conductivity boulder with high porosity identified on C-type asteroid (162173) Ryugu. *Nature Astronomy* **3**, 971-976 (2019).
9. T. Morota *et al.*, Sample collection from asteroid (162173) Ryugu by Hayabusa2: Implications for surface evolution. *Science* **368**, 654-659 (2020).
10. T. Yada *et al.*, Preliminary analysis of the Hayabusa2 samples returned from C-type asteroid Ryugu. *Nature Astronomy* **6**, 214-220 (2021).
11. S. Tachibana *et al.*, Pebbles and sand on asteroid (162173) Ryugu: On-site observation and returned particles. *Science* **375**, 1011-1016 (2022).
12. Materials and methods are available as supplementary materials.
13. A. J. Brearley, in *Meteorites and the Early Solar System II,* D. S. Lauretta, H. Y. McSween, Eds. (University of Arizona Press, 2006), pp. 587-624.
14. N. Dauphas, A. Pourmand, Thulium anomalies and rare earth element patterns in meteorites and Earth: Nebular fractionation and the nugget effect. *Geochim. Cosmochim. Acta* **163**, 234-261 (2015).
15. A.-C. Zhang *et al.*, Young asteroidal fluid activity revealed by absolute age from apatite in carbonaceous chondrite. *Nature Communications* **7**, 12844 (2016).
16. A. Morlok *et al.*, Brecciation and chemical heterogeneities of CI chondrites. *Geochim. Cosmochim. Acta* **70**, 5371-5394 (2006).
17. J. A. Barrat *et al.*, Geochemistry of CI chondrites: Major and trace elements, and Cu and Zn isotopes. *Geochim. Cosmochim. Acta* **83**, 79-92 (2012).
18. C. M. O'D. Alexander, R. Bowden, M. L. Fogel, K. T. Howard, Carbonate abundances and isotopic compositions in chondrites. *Meteorit. Planet. Sci.* **50**, 810-833 (2015).
19. J. T. Wasson, G. W. Kallemeyn, Compositions of chondrites. *Philosophical Transactions of the Royal Society of London. Series A, Mathematical and Physical Sciences* **325**, 535-544 (1988).
20. P. H. Warren: Stable-isotopic anomalies and the accretionary assemblage of the Earth and Mars: A subordinate role for carbonaceous chondrites. *Earth Planet Sci. Lett.* **311**, 93-100 (2011).
21. A. Trinquier *et al.*, Origin of nucleosynthetic isotope heterogeneity in the Solar protoplanetary disk. *Science* **324**, 374-376 (2009).
22. T. Kleine *et al.*, The non-carbonaceous–carbonaceous meteorite dichotomy. *Space Science Reviews* **216**, 55 (2020).
23. I. Leya *et al.*, Titanium isotopes and the radial heterogeneity of the solar system. *Earth Planet. Sci. Lett.*, **266**, 233-244 (2008).
24. A. N. Krot, K. Keil, E. R. D. Scott, C. A. Goodrich, M. K. Weisberg, in *Treatise on Geochemistry (Second Edition),* H. D. Holland, K. K. Turekian, Eds. (Elsevier, Oxford, 2014), pp. 1-63.
25. R. N. Clayton, T. K. Mayeda, Oxygen isotope studies of carbonaceous chondrites. *Geochim. Cosmochim. Acta* **63**, 2089-2104 (1999).
26. M. W. Rowe, R. N. Clayton, T. K. Mayeda, Oxygen isotopes in separated components of CI and CM meteorites. *Geochim. Cosmochim. Acta* **58**, 5341-5347 (1994).
27. M. Piralla *et al.*, Primordial water and dust of the Solar System: Insights from in situ oxygen measurements of CI chondrites. *Geochim. Cosmochim. Acta* **269**, 451-464 (2020).
28. Y.-f. Zheng, Calculation of oxygen isotope fractionation in metal oxides. *Geochim. Cosmochim. Acta* **55**, 2299-2307 (1991).

29. Y.-F. Zheng, Oxygen isotope fractionation in carbonate and sulfate minerals. *Geochem. J.* **33**, 109-126 (1999).
30. Y.-F. Zheng, On the theoretical calculations of oxygen isotope fractionation factors for carbonate-water systems. *Geochem. J.* **45**, 341-354 (2011).
31. Y.-F. Zheng, Calculation of oxygen isotope fractionation in hydroxyl-bearing silicates. *Earth Planet. Sci. Lett.* **120**, 247-263 (1993).
32. W. Guo, Carbonate clumped isotope thermometry: Applications to carbonaceous chondrites and effects of kinetic isotope fractionation. *Ph.D. thesis, California Institute of Technology*, 261 pp (2009).
33. R. Visser, T. John, M. Menneken, M. Patzek, A. Bischoff, Temperature constraints by Raman spectroscopy of organic matter in volatile-rich clasts and carbonaceous chondrites. *Geochim. Cosmochim. Acta* **241**, 38-55 (2018).
34. M. E. Zolensky, W. L. Bourcier, J. L. Gooding, Aqueous alteration on the hydrous asteroids: Results of EQ3/6 computer simulations. *Icarus* **78**, 411-425 (1989).
35. W. Fujiya, N. Sugiura, Y. Sano, H. Hiyagon, Mn–Cr ages of dolomites in CI chondrites and the Tagish Lake ungrouped carbonaceous chondrite. *Earth Planet. Sci. Lett.* **362**, 130-142 (2013).
36. R. Visser, T. John, M. J. Whitehouse, M. Patzek, A. Bischoff, A short-lived ^{26}Al induced hydrothermal alteration event in the outer solar system: Constraints from Mn/Cr ages of carbonates. *Earth Planet. Sci. Lett.* **547**, 116440 (2020).
37. D. P. Glavin, A. Kubny, E. Jagoutz, G. W. Lugmair, Mn-Cr isotope systematics of the D'Orbigny angrite. *Meteorit. Planet. Sci.* **39**, 693-700 (2004).
38. G. A. Brennecka, M. Wadhwa, Uranium isotope compositions of the basaltic angrite meteorites and the chronological implications for the early Solar System. *Proceedings of the National Academy of Sciences of the United States of America* **109**, 9299-9303 (2012).
39. J. N. Connelly *et al.*, The absolute chronology and thermal processing of solids in the solar protoplanetary disk. *Science* **338**, 651-655 (2012).
40. F. L. H. Tissot, N. Dauphas, T. L. Grove, Distinct ^{238}U/^{235}U ratios and REE patterns in plutonic and volcanic angrites: Geochronologic implications and evidence for U isotope fractionation during magmatic processes. *Geochim. Cosmochim. Acta* **213**, 593-617 (2017).
41. A. Trinquier, J. L. Birck, C. J. Allègre, C. Göpel, D. Ulfbeck, ^{53}Mn–^{53}Cr systematics of the early Solar System revisited. *Geochim. Cosmochim. Acta* **72**, 5146-5163 (2008).
42. L. E. Nyquist, T. Kleine, C. Y. Shih, Y. D. Reese, The distribution of short-lived radioisotopes in the early solar system and the chronology of asteroid accretion, differentiation, and secondary mineralization. *Geochim. Cosmochim. Acta* **73**, 5115-5136 (2009).
43. A. J. King, J. R. Solomon, P. F. Schofield, S. S. Russell, Characterising the CI and CI-like carbonaceous chondrites using thermogravimetric analysis and infrared spectroscopy. *Earth, Planets and Space* **67**, 198 (2015).
44. C. M. O'D. Alexander *et al.*, The provenances of asteroids, and their contributions to the volatile inventories of the terrestrial planets. *Science* **337**, 721-723 (2012).
45. C. Potiszil, R. Tanaka, K. Kobayashi, T. Kunihiro, E. Nakamura, The albedo of Ryugu: Evidence for a high organic abundance, as inferred from the Hayabusa2 touchdown maneuver. *Astrobiology* **20**, 916-921 (2020).

46. D. Jewitt, H. Hsieh, J. Agarwal, in *Asteroids IV,* P. Michel, F. E. DeMeo, W. F. Bottke, Eds. (University of Arizona Press, Tucson, 2015), pp. 221-241.
47. D. S. Lauretta *et al.*, Episodes of particle ejection from the surface of the active asteroid (101955) Bennu. *Science* **366**, eaay3544 (2019).
48. D. N. DellaGiustina *et al.*, Properties of rubble-pile asteroid (101955) Bennu from OSIRIS-REx imaging and thermal analysis. *Nature Astronomy* **3**, 341-351 (2019).
49. K. Lodders, Relative atomic solar system abundances, mass fractions, and atomic masses of the elements and their isotopes, composition of the solar photosphere, and compositions of the major chondritic meteorite groups. *Space Science Reviews* **217**, 44 (2021).
50. M. Gounelle, M. E. Zolensky, The Orgueil meteorite: 150 years of history. *Meteorit. Planet. Sci.* **49**, 1769-1794 (2014).
51. L. Baker, I. A. Franchi, I. P. Wright, C. T. Pillinger, The oxygen isotopic composition of water from Tagish Lake: Its relationship to low-temperature phases and to other carbonaceous chondrites. *Meteorit. Planet. Sci.* **37**, 977-985 (2002).
52. A. Bischoff *et al.*, The old, unique C1 chondrite Flensburg – Insight into the first processes of aqueous alteration, brecciation, and the diversity of water-bearing parent bodies and lithologies. *Geochim. Cosmochim. Acta* **293**, 142-186 (2021).
53. J. Alfing, M. Patzek, A. Bischoff, Modal abundances of coarse-grained (>5 μm) components within CI-chondrites and their individual clasts – Mixing of various lithologies on the CI parent body(ies). *Geochemistry* **79**, 125532 (2019).
54. N. Dauphas, E. A. Schauble, Mass Fractionation Laws, Mass-Independent Effects, and Isotopic Anomalies. *Annu. Rev. Earth Planet. Sci.* **44**, 709-783 (2016).
55. C. Burkhardt *et al.*, In search of the Earth-forming reservoir: Mineralogical, chemical, and isotopic characterizations of the ungrouped achondrite NWA 5363/NWA 5400 and selected chondrites. *Meteorit. Planet. Sci.* **52**, 807-826 (2017).
56. J. Sherman, The theoretical derivation of fluorescent X-ray intensities from mixtures. *Spectrochimica Acta* **7**, 283-306 (1955).
57. T. Shiraiwa, N. Fujino, Theoretical calculation of fluorescent X-ray intensities in fluorescent X-ray spectrochemical analysis. *Jpn. J. Appl. Phys.* **5**, 886-899 (1966).
58. S. Komatani, S. Ohzawa, Development of the XGT-5000 X-ray Analytical Microscope. *Readout English Edition (HORIBA Technical Reports)* **9**, 80-83 (2005).
59. Y. Abe, R. Shikaku, I. Nakai, Ancient glassware travelled the Silk Road: Nondestructive X-ray fluorescence analysis of tiny glass fragments believed to be sampled from glassware excavated from Niizawa Senzuka Tumulus No. 126, Japan. *Journal of Archaeological Science: Reports* **17**, 212-219 (2018).
60. T. Yokoyama, Y. Nagai, Y. Hinohara, T. Mori, Investigating the influence of non-spectral matrix effects in the determination of twenty-two trace elements in rock samples by ICP-QMS. *Geostandard. Geoanalytic. Res.* **41**, 221-242 (2017).
61. S. Kagami, T. Yokoyama, Simultaneous determination of insoluble fluoride-forming and high field-strength element abundances in rock samples by ICP-QMS through isotope dilution-internal standardisation. *Geostandards and Geoanalytical Research* **45**, 679-699 (2021).
62. Yokoyama et al. Multi-isotopic analyses of bulk Ryugu samples returned by the Hayabusa2 mission. *53rd Lunar and Planetary Science Conference*, The Woodlands, TX. Abstract #1273 (2022). https://www.hou.usra.edu/meetings/lpsc2022/pdf/1273.pdf

63. I. Leya, M. Schönbächler, U. Wiechert, U. Krähenbühl, A. N. Halliday, High precision titanium isotope measurements on geological samples by high resolution MC-ICPMS. *Int. J. Mass Spectrom.* **262**, 247-255 (2007).
64. G. D. Flesch, J. Capellen, H. J. Svec, in *Advanced Mass Spectrometry,* W. L. Mead, Ed. (Leiden and Son, London, 1966), vol. 3, pp. 571-581.
65. W. R. Shields, T. J. Murphy, E. J. Catanzaro, E. L. Garner, Absolute isotopic abundance ratios and the atomic weight of a reference sample of chromium. *Journal of research of the National Bureau of Standards. Section A, Physics and chemistry* **70**, 193 (1966).
66. J. Zhang, N. Dauphas, A. M. Davis, A. A. Pourmand, A new method for MC-ICPMS measurement of titanium isotope composition: Identification of correlated isotope anomalies in meteorites. *Journal of Analytical Atomic Spectrometry* **26**, 2197-2205 (2011).
67. Z. D. Sharp, A laser-based microanalytical technique for in situ determination of oxygen isotope ratios of silicates and oxides. *Geochim. Cosmochim. Acta* **54**, 1353-1357 (1990).
68. A. Pack, Isotopic traces of atmospheric O_2 in rocks, minerals, and melts. *Rev. Mineral. Geochem.* **86**, 217-240 (2021).
69. E. D. Young, A. Galy, H. Nagahara, Kinetic and equilibrium mass-dependent isotope fractionation laws in nature and their geochemical and cosmochemical significance. *Geochim. Cosmochim. Acta* **66**, 1095-1104 (2002).
70. E. D. Young, L. Y. Yeung, I. E. Kohl, On the $\Delta^{17}O$ Budget of Atmospheric O_2. *Geochim. Cosmochim. Acta* **135**, 102-125 (2014).
71. N. Kawasaki, S. B. Simon, L. Grossman, N. Sakamoto, H. Yurimoto, Crystal growth and disequilibrium distribution of oxygen isotopes in an igneous Ca-Al-rich inclusion from the Allende carbonaceous chondrite. *Geochim. Cosmochim. Acta* **221**, 318-341 (2018).
72. M. G. Śliwiński *et al.*, Secondary ion mass spectrometry bias on isotope ratios in dolomite–ankerite, Part I: $\delta^{18}O$ Matrix Effects. *Geostandards and Geoanalytical Research* **40**, 157-172 (2016).
73. K. Nagashima *et al.*, Investigation of instrumental fractionation in SIMS analyses of magnesium, silicon, and oxygen isotopes in silicates and oxides. *51th LPSC*, abstract#1719 (2020). https://www.hou.usra.edu/meetings/lpsc2020/pdf/1719.pdf
74. J. M. Huberty *et al.*, Crystal orientation effects in $\delta^{18}O$ for magnetite and hematite by SIMS. *Chemical Geology* **276**, 269-283 (2010).
75. K. P. Jochum *et al.*, Nano-powdered calcium carbonate reference materials: Significant progress for microanalysis? *Geostandards and Geoanalytical Research* **43**, 595-609 (2019).
76. R. C. J. Steele, V. S. Heber, K. D. McKeegan, Matrix effects on the relative sensitivity factors for manganese and chromium during ion microprobe analysis of carbonate: Implications for early Solar System chronology. *Geochim. Cosmochim. Acta* **201**, 245-259 (2017).
77. K. Ichimura and N. Sugiura, Preparation of synthetic dolomite for determination of Mn/Cr relative sensitivity. *46th LPSC*, abstract#1795 (2015). https://www.hou.usra.edu/meetings/lpsc2015/pdf/1795.pdf
78. P. H. Donohue, G. R. Huss, and K. Nagashima, New synthetic carbonates for investigation of manganese-chromium chronology by secondary ion mass spectrometry. *50th LPSC*, abstract#1959 (2019). https://www.hou.usra.edu/meetings/lpsc2019/pdf/1959.pdf

79. K. A.McCain, M.-C.Liu, and K. D. McKeegan, Calibration of matrix-dependent biases in isotope and trace element analyses of carbonate minerals. *J. Vac. Sci. Technol.* **B 38**, 044005 (2020).
80. P. Vermeesch, IsoplotR: A free and open toolbox for geochronology. *Geoscience Frontiers* **9**, 1479-1493 (2018).
81. A. Trinquier, J. L.Birck, C. J. Allegre, Widespread Cr-54 heterogeneity in the inner solar system. *Astrophys. J.* **655**, 1179-1185 (2007).
82. C. M. O'D. Alexander, M. Fogel, H. Yabuta, G. D. Cody, The origin and evolution of chondrites recorded in the elemental and isotopic compositions of their macromolecular organic matter. *Geochim. Cosmochim. Acta* **71**, 4380-4403 (2007).

Acknowledgments:

We thank Drae Rogers, Michael Spicuzza, and John Valley for their help with the carbonate standards for SIMS analyses. We thank SPring-8 for allowing to use their facilities. Hayabusa2 was developed and built under the leadership of Japan Aerospace Exploration Agency (JAXA), with contributions from the German Aerospace Center (DLR) and the Centre National d'Études Spatiales (CNES), and in collaboration with NASA, and other universities, institutes, and companies in Japan. The curation system was developed by JAXA in collaboration with companies in Japan. **Funding:** H. Y., T. Y., I. N., T. U., T. N., S. W., and S. T. acknowledge JSPS KAKENHI Grants. E. Y., L. N., and A. N. acknowledge NASA Grants. T. I. acknowledge Australian Research Council Grant. **Author contributions:** H. Y. coordinated coauthor contributions; led TG-MS and EMIA-Step analysis with H. H., S. K., and S. T.; and wrote the paper, with contributions from members of the Hayabusa2-initial-analysis chemistry team. T. Y. led the ICP-MS and TIMS analysis. K. N. led the SIMS analysis. I. N. led the XRF analysis. E. Y. led the LF-IRMS analysis. Y. A., J. A., C. A., S. A., Y. A., K. B., M. B., A. B., R. C., M. C., B. C., N. D., A. D.,T. R., W. F., R. F., I. G., M. H., Y. H., H. H., H. H., P. H., G. H., K. I., T. I., T. I., A. I., M. I., S. I., N. K., N. K., K. K., T. K., S. K., A. K., M. L., Y. M., K. M., M. M., K. M., F. M., A. N., L. N., M. O., A. P., C. P., L. P., L. Q., S. R., N. S., M. S., L. T., H. T., K. T., Y. T., T. U., S. W., M. W., R. W., K. Y., Q. Y., S. Y., H. Y., A. Z., and S. T. helped the analyses. All authors discussed the results and commented on the manuscript. **Competing interests:** We declare no competing interests. **Data and materials availability:** All images and data of measurement results used in this study are available at the JAXA Data Archives and Transmission System (DARTS) at https://data.darts.isas.jaxa.jp/pub/hayabusa2/paper/sample/Yokoyama_2022/. Other data on the Hayabusa2 sample are available at the DARTS archive www.darts.isas.jaxa.jp/curation/hayabusa2. The samples of Ryugu are curated by the JAXA Astromaterials Science Research Group; distribution for analysis is through an Announcement of Opportunity available at https://jaxa-ryugu-sample-ao.net. Details of the Orgueil and Ivuna samples we used for comparison are provided in the supplementary materials.

Supplementary Materials

Materials and Methods

Supplementary Text

Figs. S1 to S4

Data S1 to S9

References (*56*–*82*)

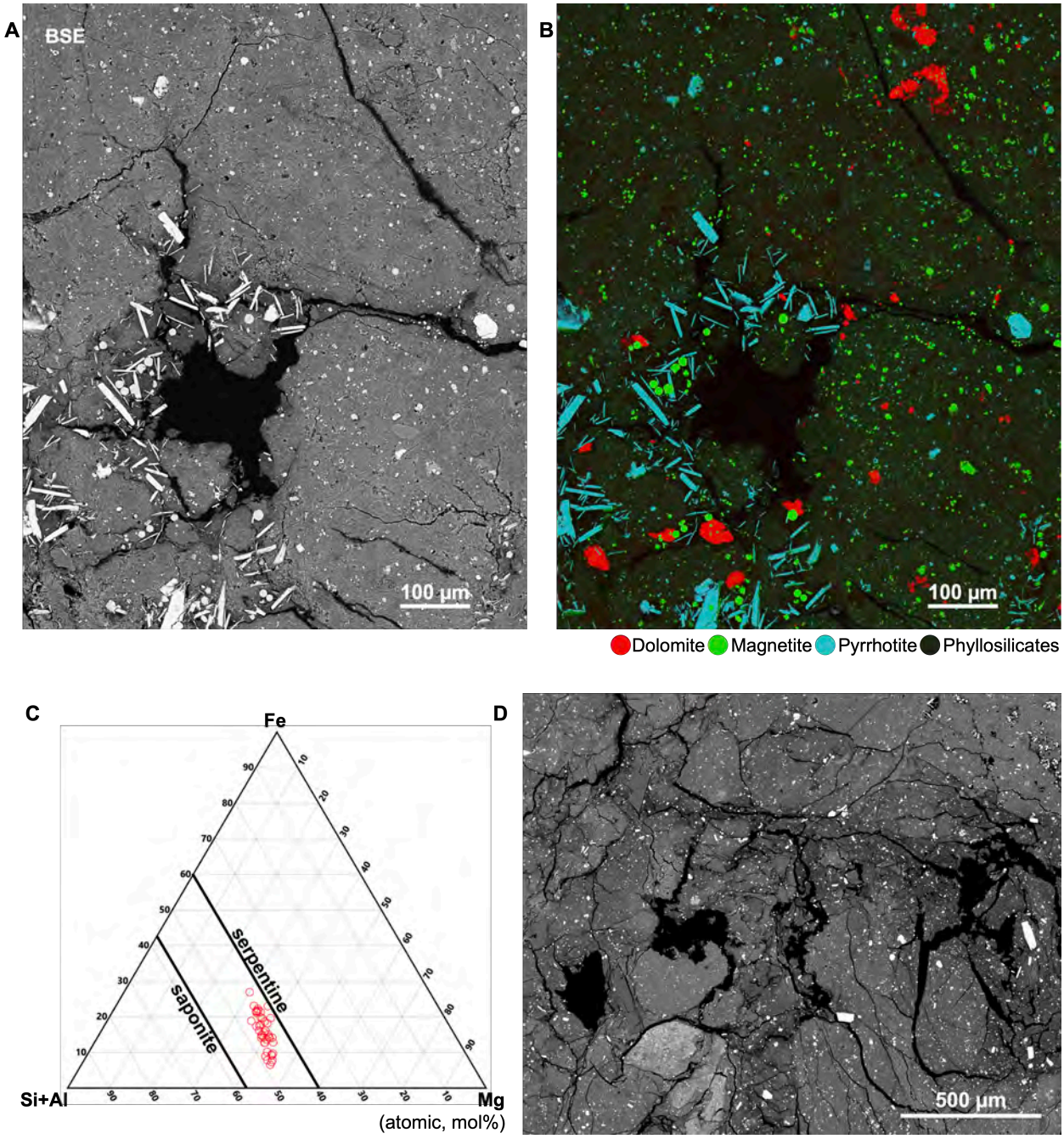

Fig. 1. Petrography of the Ryugu sample. (**A**) Backscattered electron (BSE) image. The black space in the figure is pore. (**B**) Combined elemental map by characteristic X-rays of Ca Kα, Fe Kα, and S Kα lines assigned to RGB channels of Ryugu sample A0058-C1001 (*12*), showing carbonate (dolomite), sulfide (pyrrhotite) and iron-oxide (magnetite) minerals embedded in phyllosilicates as matrix and precipitated in small veins. The sulfide texture is similar to that in the ungrouped chondrite Flensburg *(52)*. (**C**) Ternary diagram between Fe, Mg, and Si+Al showing bulk chemical compositions of phyllosilicates in A0058-C1001. Black lines are compositions of solid solution for serpentine and saponite. Each open red circle shows bulk chemical composition of phyllosilicates of various locations in Figs. 1A and 1B of 5–10 µm

square area. We chose the size of square excluding minerals other than phyllosilicates in the area. The plots show that the bulk compositions differ from place to place. The distribution shows that the phyllosilicates consist of serpentine and saponite with variable Fe/Mg ratios. Uncertainties of each point are smaller than the symbol size. (**D**) BSE image of Ryugu sample C0002-C1001, showing brecciated matrix. The texture is similar to CI chondrites *(53)*.

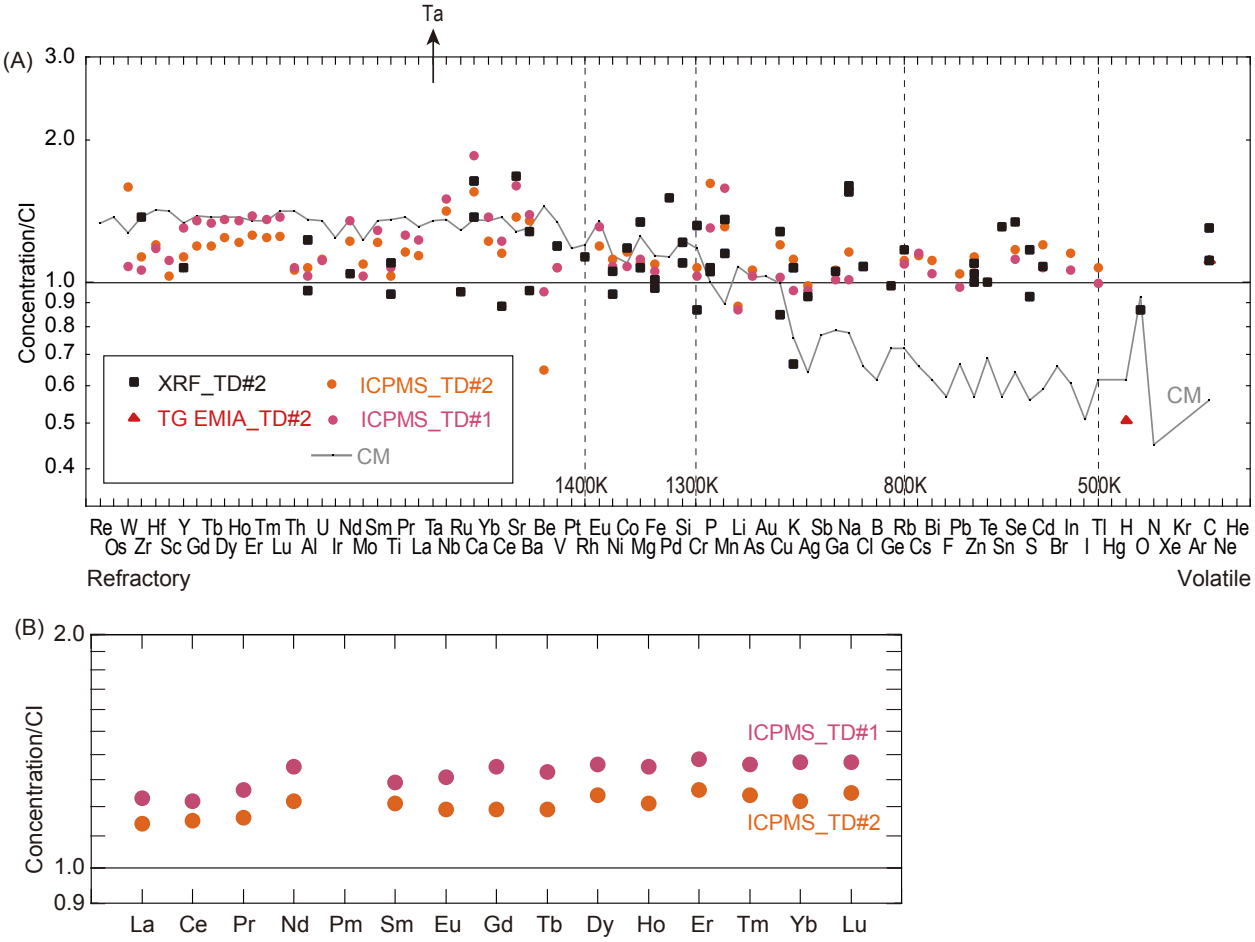

Fig. 2. Elemental abundances of Ryugu. (A) Measured abundances of elements in Ryugu normalized to CI chondrite values (*49*) plotted as a function of 50 % condensation temperature (*49*). There are no systematic trend with condensation temperature. Black squares are results from XRF analysis (*12*). Pink and orange circles are from ICP-MS analysis (*12*). Red triangles are from TG-MS and EMIA-Step analyses (*12*). TD#1 and TD#2 correspond to samples from the first and second touchdown sites, respectively. The high abundance of tantalum is indicated by upward arrow, due to contamination by the Ta projectiles used in the sampling process (*12*). The grey line shows representative values for CM (Murray-type) chondrites (*49*). The horizontal black line is the 1:1 ratio. The vertical dashed lines show condensation temperatures. **(B)** Rare Earth element abundances, plotted in order of atomic number. Numeric values and uncertainties for both panels are provided in Data S2. Uncertainties of quantified values are mostly much smaller than the observed variations among samples.

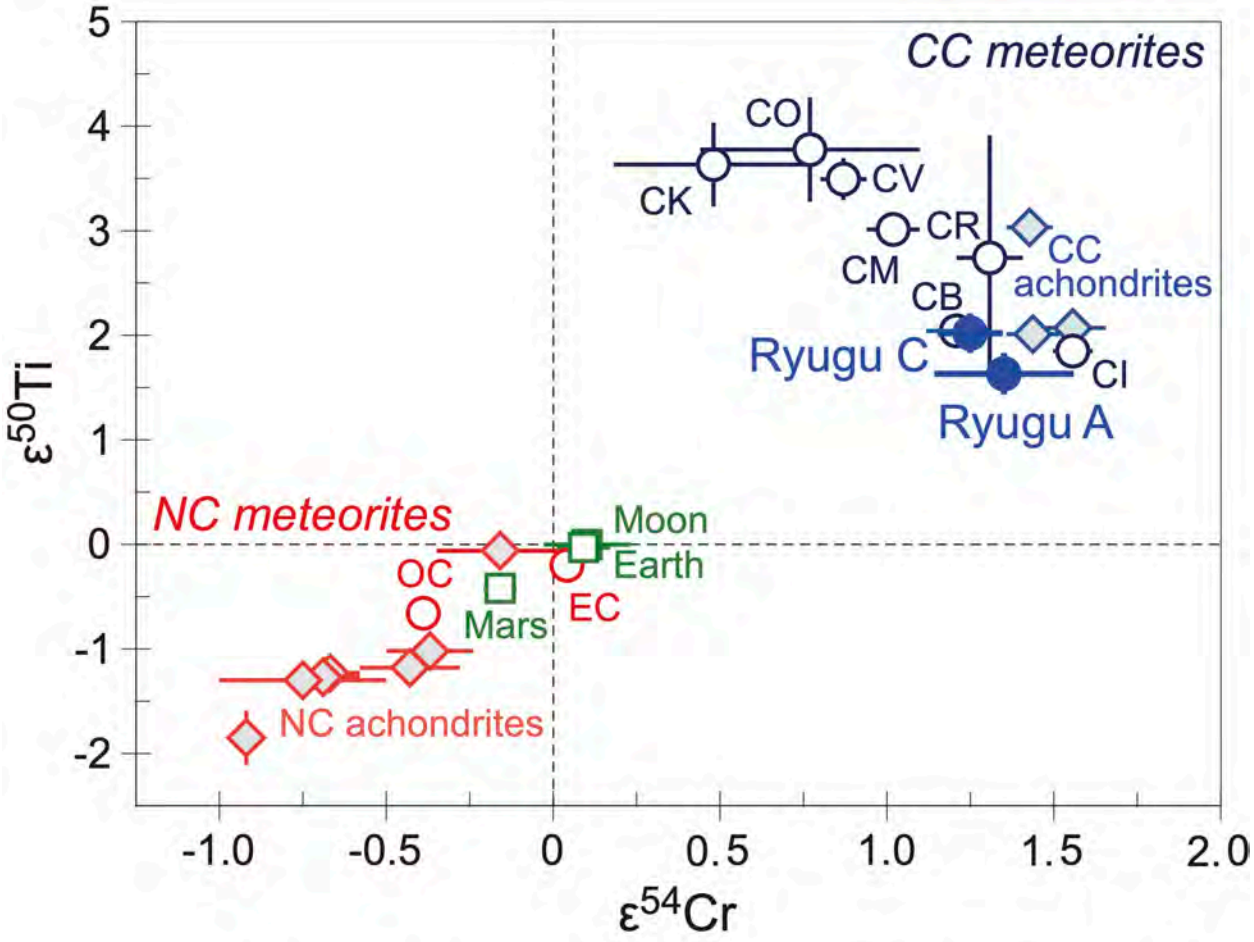

Fig. 3. Ti and Cr isotopes for Ryugu and other Solar System materials. Epsilon notations of axes are defined by Equations S1 and S2 (*12*). The Ryugu samples are most similar to the CB and CI chondrites, in the CC meteorites region. CC: Carbonaceous, NC: Non-carbonaceous. CI, CM, CO, CV, CK, CR, CB: groups of carbonaceous chondrite meteorites, OC: ordinary chondrite meteorites, EC: enstatite chondrite meteorites. The CC achondrites and NC achondrites are differentiated stony meteorites that have Ti and Cr isotopic compositions similar to CC and NC meteorites, respectively. The error bars are 2 standard deviations of the mean. Data are from (*21, 54, 55*), except Ryugu (this work). Numeric values are listed in Data S3 (*12*).

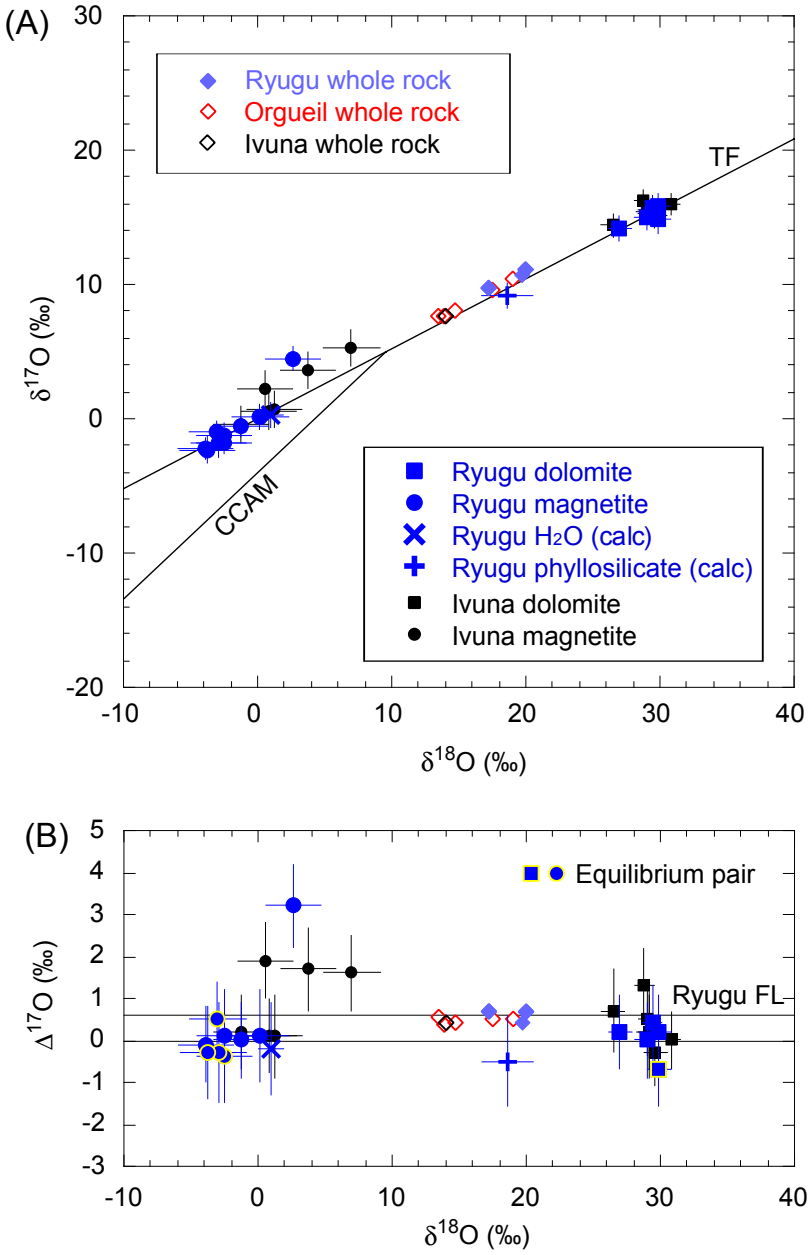

Fig. 4. Oxygen isotopes in Ryugu, Ivuna, and Orgueil. (A) $\delta^{17}O$ vs. $\delta^{18}O$. $\delta^{i}O$ (i=17 or 18) is defined as the permil deviation from the $^{i}O/^{16}O$ ratio of standard-mean-ocean-water by Equation S3 (*12*). TF: terrestrial mass fractionation line corresponding mass-dependent isotope-fractionations on Earth. CCAM: carbonaceous chondrite anhydrous mineral line corresponding mass-independent isotope-fractionations observed in refractory inclusions in chondrite meteorites. The Ryugu samples are similar to the CI chondrites. **(B)** $\Delta^{17}O$ vs. $\delta^{18}O$. $\Delta^{17}O$ is defined as the permil deviation from the TF line by Equation S4 (*12*). Ryugu FL: mass-dependent fractionation line of Ryugu fitted to the Ryugu whole rock values. Oxygen isotopic compositions of H_2O (blue × mark) and phyllosilicates (blue + mark) in samples of Ryugu were calculated from values of dolomite and magnetite (blue symbols rimmed by yellow line), which locations are shown in Figure S1 (*12*). The error bars are 2 standard deviations. Numeric values are provided in Data S4.

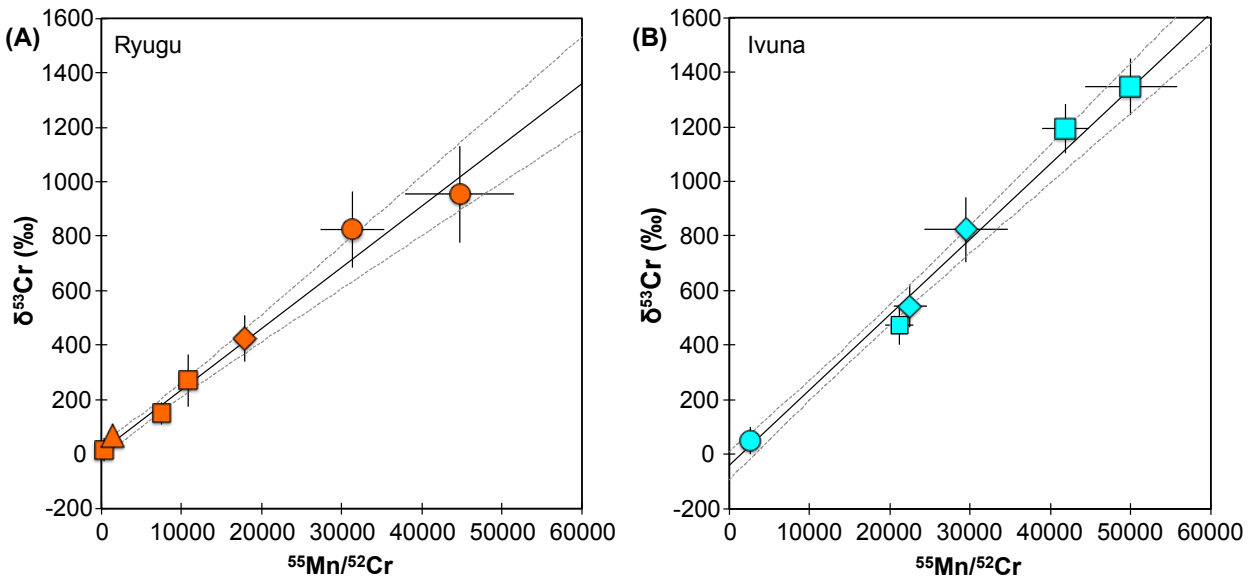

Fig. 5. ^{53}Mn-^{53}Cr isotopes for dolomite in samples of (A) Ryugu and (B) Ivuna. Each symbol shape corresponds to measurements of a single crystal. The solid straight-line is a least squares regression line and the dashed curves show 2-sigma confidence limits (*12*). The regression for Ryugu (see Supplementary Text) indicates that dolomite precipitation occurred at $5.2^{+0.7}_{-0.8}$ million years after the birth of the Solar System (there are additional systematic uncertainties on the value, see text). The error bars are 2 standard deviations. Numeric values are provided in Data S5 (*12*).

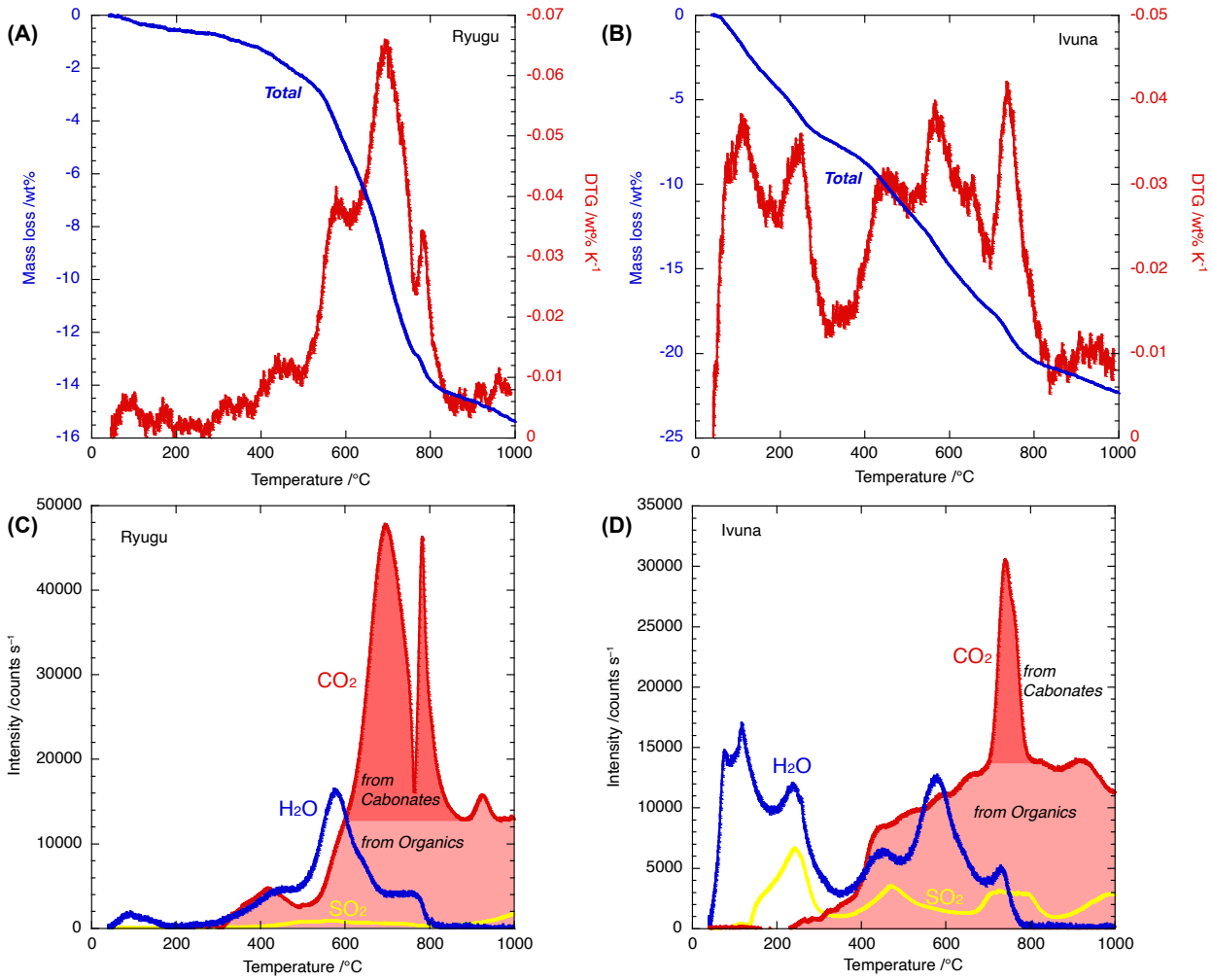

Fig. 6. Thermogravimetric analysis coupled with mass spectrometry (TG-MS) for Ryugu and Ivuna. Mass loss (blue, left axis) and differential of mass-loss (DTG; red, right axis) curves for Ryugu (**A**) and Ivuna (**B**). Derived mass intensity curves for Ryugu (**C**) and Ivuna (**D**). H_2O trace is for mass-to-charge ratio (m/z) =18, CO_2 for m/z =44, SO_2 for m/z =64. Contributions of CO_2 are assigned to carbonates (red) and organics (pink). Numeric values are provided in Data S7 (*12*).

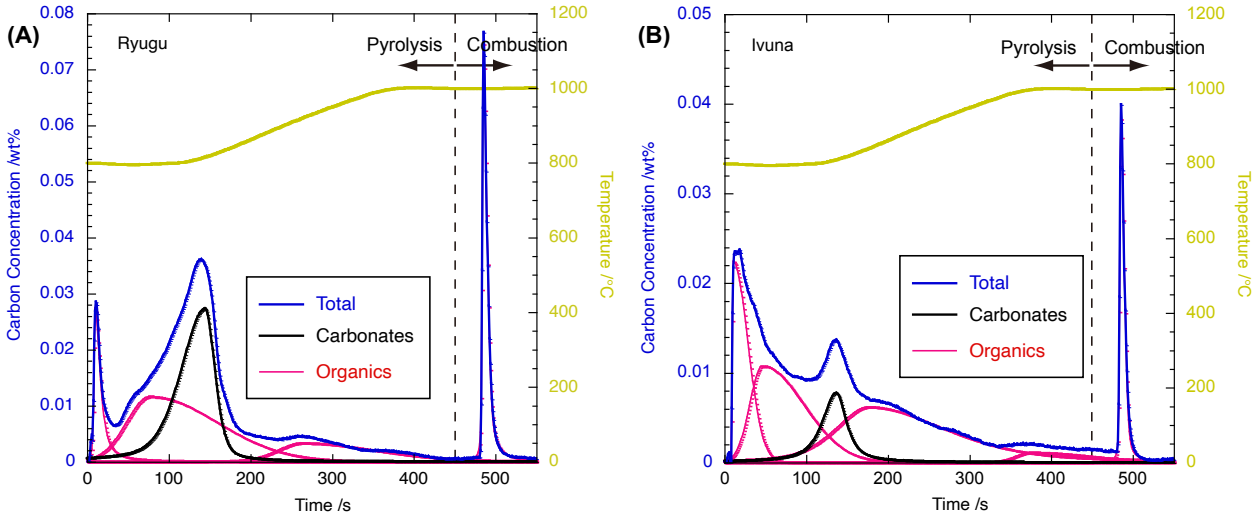

Fig. 7. Combination analyses of pyrolysis and combustion (EMIA-Step) for Ryugu and Ivuna. (A) Carbon release curve from Ryugu. **(B)** Carbon release curve from Ivuna. The carbon concentration (blue, left axis) released from sample changes with sample heating time (x-axis). The sample temperature (yellow, right axis) changes with time. The dushed line at 450 s shows the boundary between conditions of pyrolysis and combustion (*12*). The integral of bule curve corresponds to total carbon concentration in the sample. The blue curve is deconvoluted to release profiles of different carbon species (black, carbonates and pink, organics) in the sample (*12*). The integrals of the blue curve and the pink curves correspond to inorganic and organic carbon concentrations, respectively. Numeric values are provided in Data S8.

Science
AAAS

Supplementary Materials for

Samples returned from the asteroid Ryugu are similar to Ivuna-type carbonaceous meteorites

Tetsuya Yokoyama, Kazuhide Nagashima, Izumi Nakai, Edward D. Young, Yoshinari Abe, Jérôme Aléon, Conel M. O'D. Alexander, Sachiko Amari, Yuri Amelin, Ken-ichi Bajo, Martin Bizzarro, Audrey Bouvier, Richard W. Carlson, Marc Chaussidon, Byeon-Gak Choi, Nicolas Dauphas, Andrew M. Davis, Tommaso Di Rocco, Wataru Fujiya, Ryota Fukai, Ikshu Gautam, Makiko K. Haba, Yuki Hibiya, Hiroshi Hidaka, Hisashi Homma, Peter Hoppe, Gary R. Huss, Kiyohiro Ichida, Tsuyoshi Iizuka, Trevor R. Ireland, Akira Ishikawa, Motoo Ito, Shoichi Itoh, Noriyuki Kawasaki, Noriko T. Kita, Kouki Kitajima, Thorsten Kleine, Shintaro Komatani, Alexander N. Krot, Ming-Chang Liu, Yuki Masuda, Kevin D. McKeegan, Mayu Morita, Kazuko Motomura, Frédéric Moynier, Ann Nguyen, Larry Nittler, Morihiko Onose, Andreas Pack, Changkun Park, Laurette Piani, Liping Qin, Sara S. Russell, Naoya Sakamoto, Maria Schönbächler, Lauren Tafla, Haolan Tang, Kentaro Terada, Yasuko Terada, Tomohiro Usui, Sohei Wada, Meenakshi Wadhwa, Richard J. Walker, Katsuyuki Yamashita, Qing-Zhu Yin, Shigekazu Yoneda, Hiroharu Yui, Ai-Cheng Zhang, Harold C. Connolly, Jr., Dante S. Lauretta, Tomoki Nakamura, Hiroshi Naraoka, Takaaki Noguchi, Ryuji Okazaki, Kanako Sakamoto, Hikaru Yabuta, Masanao Abe, Masahiko Arakawa, Atsushi Fujii, Masahiko Hayakawa, Naoyuki Hirata, Naru Hirata, Rie Honda, Chikatoshi Honda, Satoshi Hosoda, Yu-ichi Iijima, Hitoshi Ikeda, Masateru Ishiguro, Yoshiaki Ishihara, Takahiro Iwata, Kosuke Kawahara, Shota Kikuchi, Kohei Kitazato, Koji Matsumoto, Moe Matsuoka, Tatsuhiro Michikami, Yuya Mimasu, Akira Miura, Tomokatsu Morota, Satoru Nakazawa, Noriyuki Namiki, Hirotomo Noda, Rina Noguchi, Naoko Ogawa, Kazunori Ogawa, Tatsuaki Okada, Chisato Okamoto, Go Ono, Masanobu Ozaki, Takanao Saiki, Naoya Sakatani, Hirotaka Sawada, Hiroki Senshu, Yuri Shimaki, Kei Shirai, Seiji Sugita, Yuto Takei, Hiroshi Takeuchi, Satoshi Tanaka, Eri Tatsumi, Fuyuto Terui, Yuichi Tsuda, Ryudo Tsukizaki, Koji Wada, Sei-ichiro Watanabe, Manabu Yamada, Tetsuya Yamada, Yukio Yamamoto, Hajime Yano, Yasuhiro Yokota, Keisuke Yoshihara, Makoto Yoshikawa, Kent Yoshikawa, Shizuho Furuya, Kentaro Hatakeda, Tasuku Hayashi, Yuya Hitomi, Kazuya Kumagai, Akiko Miyazaki, Aiko Nakato, Masahiro Nishimura, Hiromichi Soejima, Ayako Suzuki, Toru Yada, Daiki Yamamoto, Kasumi Yogata, Miwa Yoshitake, Shogo Tachibana, Hisayoshi Yurimoto*

Correspondence to: yuri@ep.sci.hokudai.ac.jp

This PDF file includes:

Materials and Methods
Supplementary Text
Figs. S1 to S4
Captions for Data S1 to S9

Materials and Methods

Samples

Ryugu samples from the first touchdown site (small grain aggregates catalogued as A0106 (15.7 mg of the total 38.4 mg), A0107 (31.0 mg) and individual grains A0040 (3.0 mg), A0058 (3.3 mg), A0094 (1.8 mg)) and second touchdown site (small grain aggregates catalogued as C0107 (12.9 mg of the total 38.8 mg), C0108 (33.0 mg) and individual grain C0002 (28.8 mg of the total 93.5 mg)) were allocated in this study (Fig. S3). The small grain aggregate samples (A0106, A0107, C0107, C0108) consist of grains less than ~1 mm. The grain C0002 is the third largest grain among the samples returned by Hayabusa2. Grains A0040 and C0002 have rugged surfaces. Grain A0058 has smooth surface. Grain A0094 show elongated blocklike morphology. Preparations for each sample are described in each measurement method described below. Most of these Ryugu samples have been consumed in this study, but the rests not consumed will be returned to Institute of Space and Astronautical Science of Japan Aerospace Exploration Agency in June 2022. The returned samples will be available at the DARTS archive www.darts.isas.jaxa.jp/curation/hayabusa2 from August 2022.

Samples of the CI chondrites were used for comparison. We obtained samples of Ivuna from the Natural History Museum, UK, and the University of Göttingen, Germany; and Orgueil from the University of California, Los Angeles, USA, and the University of Göttingen, Germany, were used as references. Samples of the CV chondrite Allende from Hokkaido University, Japan, was used to make a standard for carbon content measurements of X-ray fluorescence analysis. These meteorite samples have been consumed in this study.

X-ray fluorescence (XRF) analysis

Ryugu samples from C0108 were used for XRF analysis. We have set the samples in an aluminum sample holder and used it for all XRF measurements in this study. The C0108 Ryugu sample was gently ground with a mortar and pestle made of quartz glass to a grain-size of approximately 10 μm. Subsequently, we carefully loaded 24 mg of powder into the sample cell. The sample cell is a 6 mm diameter hole drilled in a 0.6 mm thick acrylic plate. A thin PET film underneath the plate holds the sample in place. We then gently compacted the sample by hand with another flat acrylic plate. After sample loading, the cell was covered by a second piece of polyethylene terephthalate (PET) film. When we conducted XRF analysis at Rigaku and Horiba companies, the upper PET film was removed before placing the sample in the instruments. When we conducted XRF analysis at SPring-8 synchrotron facility, the upper PET film was not removed.

The concentrations of major and minor elements, including carbon, in the Ryugu samples were determined by X-ray fluorescence analysis using a wavelength-dispersive X-ray spectrometer (WDX). The Ryugu sample analysis was performed with a Rigaku ZSX Primus IV sequential WDXRF in the Osaka factory of the Rigaku Corporation. The instrument has overhead X-ray irradiation optics with a 4 kW Rh anode X-ray tube. A gentle evacuation procedure was applied that makes it possible to perform evacuation and leak sequences without scattering any particles from a non-pressed powder sample during the sample loading and unloading. The evacuation speeds were adjusted by analog rock powder samples finer than the Ryugu sample. We measured the concentration of 20 major and minor elements in the Ryugu sample: C, O, Na, Mg, Al, Si, P, S, Cl, K, Ca, Ti, V, Cr, Mn, Fe, Co, Ni, Cu and Zn. All measurements used a 3 mm diameter collimator mask and the voltage and current of the X-ray

tube were optimized to each element as follows: 30 kV-100 mA for C to Cl, 40 kV-75 mA for K to Ti, 50 kV-60 mA for V to Mn and 60 kV-50 mA for Fe to Zn. The pressure in the sample chamber was maintained at 13 Pa throughout the measurement of all elements. The total counting time was about 24 minutes for the 20 elements.

The quantitative elemental abundances were determined using the fundamental parameter (FP) method (*56, 57*), because matrix-matched reference materials were not available for Ryugu samples. Fifty reference standards, including commercially available geological standards, ore standards, metal standards and pure reagents (Data S9), were used to establish the FP sensitivity calibration curves for the 20 elements. These reference standards were loaded into the sample cell in the same manner as the Ryugu sample and measured. The sensitivity curves of carbon and oxygen were obtained by measuring ferroalloy reference materials and pure oxide reagents, respectively.

X-ray fluorescence analysis using an energy-dispersive X-ray spectrometer (EDS) was performed with a HORIBA XGT-9000 X-ray Analytical Microscope at the Horiba Techno Service Co., Ltd., Kyoto, Japan (*58*). The sample cell was loaded into the measurement position in vacuum. The primary X-rays, focused to 100 μm in diameter with a polycapillary, vertically irradiated the sample, and fluorescence X-rays from the sample were measured with the silicon drift EDS detector at an angle of 45°. The primary X-rays were scanned over an area of 3.072 × 3.072 mm by moving of the sample cell at a step size of 24 μm to compensate for any sample heterogeneities in the cell. A Rh target X-ray tube was used to generate the primary X-rays. The measurement conditions of the X-ray tube voltages and currents were set to 30 kV and 250 μA, respectively. The measurement time and X-ray working distance was set to 60 ms per pixel and 1.0 mm, respectively. The standard FP method was applied to quantify the following elements: Na, Mg, Al, Si, P, S, K, Ca, Ti, V, Cr, Mn, Fe, Ni, Cu and Zn, using the geological reference sample JSd-2 as a standard. Quantification of the C contents was performed by the calibration curve method. Two standard samples with known C contents were prepared for the calibration. The standard samples were mixtures of powdered Allende CV3 chondrite and graphite powder. The Allende powder was preheated at 1000 °C in air to remove carbon before mixing with the graphite. The carbon concentrations in the two standards were quantified by EMIA-Step and were 0.00 wt.% and 4.79 wt.%, respectively.

The heavy element compositions of the Ryugu sample were determined by high-energy (HE) synchrotron radiation (SR) XRF analyses at two beamlines in SPring-8, the Japan Synchrotron Radiation Research Institute (JASRI). The beamlines used were BL37XU, a hard X-ray undulator beamline mainly used for X-ray micro/nano-spectrochemical analysis, and BL08W, a wiggler beamline, that provides higher energy X-rays. Monochromatic X-rays were obtained with crystal monochromators and their energy was set to 37.5 keV for the experiment at the BL37XU, and 116.0 keV for BL08W. For both beamlines, the incident X-ray beams were prepared by adjusting a four-quadrant slit to 500 μm (vertical) × 500μm (hirizontal). The XRF spectra were measured with a Ge solid state detector at 90° to the incident X-ray beam for 600 s or 1800 s in live time, for measurements at BL37XU and BL08W, respectively. Six spots on the Ryugu sample were measured at the BL37XU, while three spots were measured at the BL08W. Eight standard samples consisting of certified reference materials of silicate glass (NIST SRM 610, 612, and 614) and geological standard samples (JG-1, JGb-1, JP-1, JR-2, and JSy-1) were prepared to calibrate concentration and calculate detection limit for each element (*59*). We obtained sensitivity coefficients from the standards for 32 heavy elements: Ga, Ge, Se, Rb, Sr, Y,

Zr, Ru, Rh, Pd, Ag, Cd, In, Sn, Te, Ba, La, Ce, Pr, Nd, Sm, Eu, Gd, Tb, Dy, Ho, Er, Tm, Yb, Lu, Hf, and Ta. Several other elements (As, Nb, Mo, In, Sb, Cs, and W) were excluded from the analysis due to interferences with peaks from the background materials or overlapping with scattered X-rays. All SR measurements were conducted nondestructively under atmospheric pressure.

Acid digestion

The aggregate sample A0106 (15.7 mg) was separated into two types of samples: one (1.6 mg) was intact portion and another portion (14.1 mg) was reserved for soluble organics extraction experiments. The intact portion was mixed with 27 mg of the aggregate sample A0107 (hereafter A0106+A0107). The Ryugu aggregate samples, A0106+A0107 and C0108, were used for destructive analyses of elemental abundances and isotopic compositions in bulk Ryugu samples. The sample A0106+A0107 was a powdered material prepared from a mixed aggregate of A0106 (1.6 mg) and A0107 (27 mg), while C0108 was the powdered sample in the XRF sample cell retrieved after the XRF analytical session. All of the sample digestion and chemical separation procedures were conducted in a class-100 clean laboratory at Tokyo Institute of Technology (Tokyo Tech). The two samples, 24 mg of A0106+A0107 and 22 mg of C0108, were weighed in clean Teflon vials, and a mixture of HF and HNO_3 was added. The vials were tightly capped, agitated in an ultrasonic bath for 30–60 min, and heated at 120 °C on a hotplate for 12 h. Then, the vials were continuously heated on the hot plate at 180 °C for 3 to 4 days until the color of the sample and solution change from black to white and from dark reddish-brown to pale yellow, respectively. After sample dissolution, the vials were opened, and the sample solutions were dried at 120 °C. The samples were heated in closed vials with a mixture of HNO_3 and HCl at 120 °C for 12 h, and then dried at 120 °C. Subsequently, the samples were treated in closed vials with a mixture of HNO_3 and H_2O_2 to facilitate the decomposition of organic matter. After the final treatment with HNO_3, the samples were dissolved with 5 mL of 0.5 M HNO_3.

Inductively coupled plasma mass spectrometry (ICP-MS) for elemental analysis

The total mass of the dissolved sample solution was weighed. Then, 0.8 %, 2.4 %, and 4.8 % aliquots of the solution were weighed into three clean sample tubes for the measurements of Group-1 (Na, Mg, Al, P, K, Ca, Cr, Mn, Fe, Co, and Ni), Group-2 (Ti, Zr, Nb, Mo, Hf, Ta, and W), and Group-3 (Li, Be, Sc, V, Cu, Zn, Ga, As, Se, Rb, Sr, Y, Ag, Cd, In, Cs, Ba, La, Ce, Pr, Nd, Sm, Eu, Gd, Tb, Dy, Ho, Er, Tm, Yb, Lu, Tl, Pb, Bi, Th, and U) elements. An appropriate amount of Rh (60 ng) was added to the Group-1 sample tube as an internal standard, and the sample solution was diluted with 0.5 M HNO_3 to make the dilution factor (DF) to be 20000 for the measurement of P, K, Ca, and Co. A portion of this solution was diluted by a factor of 10 with 0.5 M HNO_3 (DF = 200000) for the measurement of Na, Mg, Al, Cr, Mn, Fe, and Ni. A mixture of spike solutions enriched in ^{49}Ti (96.25%), ^{91}Zr (94.59%), ^{97}Mo (94.19%), ^{179}Hf (86.87%), and ^{182}W (94.07%) was added to the Group-2 sample tube for isotope dilution analyses. The amounts of individual spikes added to the sample are as follows: Ti = 250 ng, Zr = 5 ng, Mo = 0.5 ng, Hf = 0.5 ng, W = 0.5 ng. The sample solution was diluted and conditioned to be 0.5 M HNO_3–0.05 M HF (DF = 4000) because the Group-2 elements are not stable in the solution without F^- ion as they hydrolyze. For the Group-3 sample, a mixture of spike solutions enriched in ^{113}In (89.76%) and ^{203}Tl (97.09%) was added, and the spiked sample solution was diluted with 0.5 M HNO_3 (DF = 5000). The amounts of In and Tl spikes added to the sample are 0.7 ng and 0.7 ng, respectively.

The measurement of elemental abundances in the sample solutions was conducted with a quadrupole-type ICP-MS instrument (X-series 2, Thermo Fisher Scientific) installed at Tokyo Tech. The analytical conditions of ICP-MS are summarized in Data S1. All of the ICP-MS measurements were performed in a normal solution mode without collision cell. The measured isotopes for individual elements were selected to minimize the influence of spectral interferences including oxides and doubly charged ions. Of the spectral interferences, oxides (Data S1) were corrected by following previously established procedure (*60*). Influences were < 2 % in most cases. Exceptions are ^{55}MnO on ^{71}Ga (~17 %), ^{59}CoO on ^{75}As (~6 %), ^{91}ZrO on ^{107}Ag (~5 %), ^{141}PrO on ^{157}Gd (~7 %), and ^{143}NdO on ^{159}Tb (~3 %).

For the measurement of Group-1 elements, we used a multi-elemental solution XSTC-13 (SPEX CertiPrep, USA) and a single element P solution (Fujifilm-Wako) as the standards. Additionally, a single element Ca solution (Fujifilm-Wako) was used for a standard because measurement of ^{44}Ca in XSTC-13 was hampered by the coexisting Sr in the solution which formed doubly charged ion $^{88}Sr^{2+}$. With these standards, the abundances of Group-1 elements in the Ryugu samples were determined by the calibration curve method with ^{103}Rh internal standardization. For the measurement of Group-2 elements, a custom-made multi-elemental solution XSTC-4043-100 (SPEX CertiPrep, USA) was used for a standard. The abundances of Ti, Zr, Mo, Hf, and W in the Ryugu samples were determined by the isotope dilution method while those of Nb and Ta were determined by internal standardization using the signals of ^{91}Zr and ^{179}Hf (*61*). For the measurement of Group-3 elements, XSTC-13 and another multi-elemental solution XSTC-1 (SPEX CertiPrep, USA) were used as standards. The abundances of In and Tl were determined by the isotope dilution method while those of the other Group-3 elements were determined by internal standardization using the signals of ^{113}In and ^{203}Tl (*60*). The abundances of Pb were determined by considering the non-terrestrial Pb isotopic compositions in the Ryugu samples (*62*). The analytical uncertainties of the determined elemental abundances were estimated by the propagation of uncertainties associated with the signal intensities and the concentrations of standards or spikes. The incorporation of chemical blanks was evaluated two times and corrected by subtracting the total analytical blank values, but the contributions to the total uncertainties were negligible (< 1 %) except for Mo (~2 %).

Chemical separation for isotopic measurements of titanium and chromium

The 80 % aliquots of the dissolved A0106+A0107 and C0108 samples were used for isotopic analyses of Cr and Ti with Thermal ionization mass spectrometry (TIMS) and Multi-collector (MC)-ICP-MS, respectively. The sample solution was dried and treated with HBr to convert the chemical form, which was then dissolved with 1 mL 1.5 M HBr. The solution was loaded onto 0.1 mL of an anion exchange resin (AG1-X8, 200–400 mesh, BioRad) charged in a polyethylene column. Most of the elements were collected with the subsequent elution of 0.45 mL 1.5 M HBr, followed by the collection of Zn with 1.5 mL 0.2 M HBr–0.5 M HNO_3 and Pb with 1.5 mL H_2O.

After drying down the first cut of the Pb column chemistry, a 0.3 mL of a pure Al solution (10000 μg mL^{-1}) was added. This is to convert the chemical composition of the sample to be Ca/(Ca + Al) < 0.43 and Mg/(Mg + Al) < 0.4, to avoid the incorporation of Ti, Zr, and Hf into insoluble fluorides (*61*). The sample was dried and treated with HNO_3 and HF to convert the chemical form. Then, it was dissolved with 1 mL 0.4 M HCl–0.5 M HF and centrifuged at 10000 rpm for 20 min to separate any insoluble fluorides. The supernatant was loaded onto the anion exchange resin AG1-X8 in a 1 mL polypropylene column. After the sample loading, 3 mL of 0.4

M HCl–0.5 M HF was eluted to collect major elements. Subsequently, Ti, Zr, and Hf were collected by eluting 5 mL 9 M HCl–0.05 M HF, followed by the collection of W and Mo with 10 mL 9 M HCl–1 M HF and 5 mL of 6 M HNO_3–3 M HF, respectively. The second cut containing Ti, Zr, and Hf was dried and dissolved with 0.5 mL 8 M HNO_3–0.2 M HF, which was loaded onto 0.5 mL of an extraction chromatographic resin "DGA-Normal Resin" (50–100 μm, Eichrom Technologies Inc, USA) filled in a polypropylene column. Then, Ti was collected with 2.0 mL elution of 8 M HNO_3–0.2 M HF, followed by the collection of Zr and Hf with 6.0 mL 0.5 M HF. The Ti fraction was further purified by repeating the initial Ti chemistry procedure with a reduction in column size and eluant volume to 30 % of the initial size. The overall recovery of Ti was > 90 %.

The major element fraction obtained in the initial Ti chemistry was merged with the insoluble fluoride residue that was not loaded onto the column. The mixture was dried and attacked with HNO_3 twice and 12 M HCl, then dissolved with 1 mL 6 M HCl. The solution was loaded onto the 1 mL anion exchange resin that was used in the Ti chemistry, followed by the elution of 3.0 mL 6 M HCl to collect major elements excluding Fe. Subsequently, 4.0 mL 0.1 M HNO_3 was eluted to collect Fe and U. The first cut of Fe-U chemistry was dried and attacked by HNO_3, and then it was dissolved with 0.5 mL 4 M HNO_3. The sample solution was loaded on a 0.3 mL "Sr Resin" (50–100 μm, Eichrom Technologies Inc, USA) placed on a 0.3 mL "RE Resin" (50–100 μm, Eichrom Technologies Inc, USA), followed by the elution of 1.0 mL 4 M HNO_3 to collect major elements. Then, the tandem columns were disassembled. For the column filled with RE resin, 1.0 mL 6 M HNO_3 was eluted to collect remaining major elements, which was merged into the same vial containing major elements. Then, 3.5 mL 0.1 M HCl–0.3 M HF was eluted to collect REEs and Th. For the column filled with Sr resin, 6.5 mL 8 M HNO_3 and 4.0 mL H_2O were eluted to collect Ba and Sr, respectively.

The major element fraction obtained in the Sr chemistry was dried and then dissolved with 1 ml 1 M HNO_3–10 % H_2O_2 and it was left overnight at room temperature. In this step, an 1.8 mL column filled with the DGA-Normal Resin was placed on the top of a cation exchange resin (1 : 1 mixture of AG50W-X8 200–400 mesh and AG50W-X12 200–400 mesh, BioRad) in an 1 mL polypropylene column. The sample solution was loaded onto the top of the tandem column, followed by the elution of 7.0 ml 1 M HNO_3. The 1.8 ml column was removed at this point, and then 16 mL 1 M HNO_3 and 2 mL 0.5 M HF were successively eluted onto the mixed cation exchange resin to collect major cations (e.g., Na, Mg and Ni) and Al, respectively. Next, Cr was collected by the elution of 4.0 ml 6 M HCl. The overall recovery of Cr was ~90 %. For the column filled with 1.8 mL DGA-Normal Resin, 4.0 ml 10 M HNO_3 was eluted to collect Ca.

Titanium isotopic analysis with MC-ICP-MS

The Ti isotopic compositions in the Ryugu samples were measured by a MC-ICP-MS instrument (Neptune-Plus; Thermo Fisher Scientific) installed at the University of Tokyo. The separated Ti fraction was dried and dissolved in 0.5 M HNO_3–0.001 M HF to a concentration of 150 ng/mL. The dissolved sample was introduced into the MC-ICP-MS using a Cetac Aridus II micro-concentric desolvating nebulizer with an uptake rate of ~0.15 mL/min. Measurements were performed using a Jet sample cone and an X skimmer cone with high mass resolution, which resulted in ^{48}Ti signal intensities of ~2.5×10^{-10} A. All five Ti isotopes together with ^{43}Ca, ^{51}V and ^{53}Cr were monitored in dynamic mode using Faraday cups connected to 10^{11} Ω amplifiers. Data were acquired from 40 cycles, 2 lines/cycle, 8.4 s integration/line, and 4 s idle time between lines. Instrumental mass fractionation was corrected relative to ^{49}Ti/^{47}Ti =

0.749766 (*63*) with an exponential law. Isobaric interferences on Ti isotopes from ^{46}Ca, ^{48}Ca, ^{50}V, and ^{50}Cr were corrected for assuming that the mass bias factors of Ca, V, and Cr were identical to that of Ti. For the correction, the literature values of ^{50}V/^{51}V = 0.0251 (*64*) and ^{50}Cr/^{53}Cr = 0.45732 (*65*) were utilized, whereas Ca isotope ratios were artificially modified to ^{46}Ca/^{43}Ca = 0.02365 and ^{48}Ca/^{43}Ca = 1.4039 which eliminate artificial isotopic anomalies for Ca-doped Ti standard solutions with Ca/Ti ratios of 1–5. Individual sample measurements were bracketed by analyses of a NIST SRM 3162a standard solution. The Ti isotopic ratios of samples were determined relative to the standard runs. It has previously been shown that NIST SRM 3162a has an 0.28 ± 0.17 excess of ^{50}Ti relative to Alfa Aesar Ti standard solution that is widely used in meteorite Ti isotope studies (*66*). For comparison with literature values, sample ^{50}Ti/^{47}Ti ratios are reported in the ε unit defined as:

$$\varepsilon^{50}\mathrm{Ti} = \left(\frac{^{50}\mathrm{Ti}/^{47}\mathrm{Ti}_{\mathrm{sample}}}{^{50}\mathrm{Ti}/^{47}\mathrm{Ti}_{\mathrm{NIST3162a}}} - 1\right) \times 10^4 + 0.28. \qquad \text{(S1)}$$

Analytical uncertainties on sample Ti isotope ratios combined the internal precisions (2 standard error (SE)) and the dispersion of the mean of the bracketing standard analyses (2SE), added in quadrature.

Chromium isotopic analysis with TIMS

The Cr isotopic compositions in the Ryugu samples were measured by a TIMS instrument (Triton-Plus; Thermo Fisher Scientific) installed at Tokyo Tech. The instrument was equipped with eight movable Faraday cups and one center Faraday cup, which were all connected with 10^{11} Ω amplifiers with a dynamic range of 50 V. NIST SRM 979 was used as a Cr isotopic reference material. The Cr sample (2.5–3.0 μg per single analysis) was loaded onto the center of a prebaked single W filament together with Al and B-doped silica gel as an activator. The filament was first heated to 1000 °C, followed by the gentle heating of the filament until a stable Cr^+ beam was obtained at ~1200 °C. The typical beam intensity of $^{52}Cr^+$ at the beginning of the data acquisition was 1.5×10^{-10} A. The isotopic ratios of Cr (^{50}Cr/^{52}Cr, ^{53}Cr/^{52}Cr, and ^{54}Cr/^{52}Cr) were acquired by dynamic multicollection and multistatic methods with a three-line cup setting. The effect of mass fractionation during the TIMS measurement was corrected with the exponential law by assuming that ^{50}Cr/^{52}Cr = 0.051859 (*65*). The spectral interferences on Cr isotopes (^{50}Ti, ^{50}V, and ^{54}Fe) were corrected by monitoring ^{49}Ti, ^{51}V, and ^{56}Fe. The Cr isotope data were reduced by averaging 420 ratios (2 standard deviation (SD) rejection level = 4.55 %), acquired from 21 blocks of 20 cycles/block, 3 lines/cycle, and 16.667 s integration/line. A single isotopic measurement required 10 h, including the filament heating time. The ^{54}Cr/^{52}Cr isotopic ratios in Ryugu samples are reported in the ε unit:

$$\varepsilon^{54}\mathrm{Cr} = \left(\frac{^{54}\mathrm{Cr}/^{52}\mathrm{Cr}_{\mathrm{sample}}}{^{54}\mathrm{Cr}/^{52}\mathrm{Cr}_{\mathrm{NIST979}}} - 1\right) \times 10^4. \qquad \text{(S2)}$$

Analytical uncertainties for the Ryugu samples are either the 2 SD of multiple sample measurements or the largest analytical uncertainty in multiple campaigns of NIST SRM 979 measurements, whichever is larger.

Laser-fluorination isotope-ratio mass-spectrometry (LF-IRMS)

The A0107 and C0002 Ryugu samples were used for LF-IRMS analyses at UCLA and University of Göttingen (UG), respectively.

Methods at UCLA

Two aliquots from A0107 were analyzed, with masses of 1.50 mg (sample B) and 2.58 mg (sample C), respectively. In addition, three aliquots of the Orgueil CI chondrite (3.06 mg, 4.27 mg, and 4.31 mg) were analyzed using the same methods for comparison. The samples of Ryugu and Orgueil were chips of 1 to 2 and 3 to 6 pieces per aliquot, respectively, in order to simulate the material that we were analyzing from Ryugu. Samples were loaded into the vacuum chamber for analysis with a baseline pressure of ~ 5×10^{-7} mbar. The samples were then heated with an infrared lamp while actively pumping to drive off any adsorbed water. Heating duration was approximately 3 hours. The temperature of the samples inside the chamber during heating was ~110 to 120 ˚C as deduced by thermal imaging of analogous CI meteorite samples through the ZnSe window of the chamber under identical conditions.

Laser-heating assisted fluorination was used to liberate O_2 for isotopic analysis. 90 mbar of F_2 gas was used as the fluorinating agent. The F_2 was purified by double distillation using $KNiF_6$·KF salt as a thermally activated source and sink for the fluorine gas. Blank oxygen was below detection. The heating laser is a 20 W CO_2 laser (10.6 μm) (*67*) gated with a pulse frequency of 10 Hz. The duration of the laser heating was about 15 minutes for each sample. Following fluorination, the product gas was purified in the vacuum system by passing through a trap warmed to 110 ˚C containing granules of optical-grade KBr (to passivate excess F_2) between two cryogenic traps (cooled with liquid N_2) to remove SiF_4 from the fluorination process, Br_2 from the fluorine trap, and any other condensable gaseous products. The liberated O_2 gas was trapped on a glass cryotrap (liquid N_2 temperature) filled with 13X molecular sieve for 60 minutes, then heated to 210 ˚C for 30 minutes to allow expansion into a calibrated volume for measuring the recovered moles of gas. The purified O_2 was trapped again at liquid N_2 temperature on silica gel for transport to the mass spectrometer.

Isotope ratios were determined by measuring $^{32}O_2^+$, $^{33}O_2^+$, and $^{34}O_2^+$ (as well as $^{36}O_2^+$) on a high-mass-resolution, double-focusing gas-source mass spectrometer at UCLA (Nu Instruments Panorama 001). The mass resolving power defined as mass M over difference of mass ΔM ($M/\Delta M$) of 40,000 used for these measurements is sufficient to resolve mass interferences, including trace NF^+ that is a potential mass spectrometric isobar for $^{33}O_2^+$ (i.e., $^{17}O^{16}O^+ + {}^{16}O^{17}O^+$). The $^{32}O_2^+$, $^{33}O_2^+$, and $^{34}O_2^+$ ion beams were measured using Faraday cups with amplifier resistors of 10^{10} Ω, 10^{13} Ω, and 10^{11} Ω, respectively. Analyses were obtained from 6 and 3 blocks for samples C and B, respectively, with each block comprising 30 cycles of sample/reference gas comparisons, and each measurement in a cycle consisting of 30 s integrations.

The reference gas was calibrated using O_2 purified by gas-chromatography from air, and O_2 liberated by fluorination using the same procedures as those outlined above. We report $^{18}O/^{16}O$ and $^{17}O/^{16}O$ relative to standard mean ocean water (SMOW) as δ values (permil deviations from the standard) in which

$$\delta^{18}O_{SMOW} = 10^3((^{18}O/^{16}O)_{Sample}/(^{18}O/^{16}O)_{SMOW} - 1) \quad \text{(S3)}$$

and similarly for $\delta^{17}O_{SMOW}$. We calculate the deviations in $^{17}O/^{16}O$ for a given $^{18}O/^{16}O$ value from the terrestrial oxygen rock reservoir using the cosmochemical definition

$$\Delta^{17}O = \delta^{17}O_{SMOW} - 0.52 \times \delta^{18}O_{SMOW}, \quad \text{(S4)}$$

with 0.52 representing mass-dependent fractionation. San Carlos olivine (SC olivine), a commonly used reference for rock and mineral oxygen isotope analyses, has a $\Delta^{17}O$ of ~ –0.05 to –0.1 ‰ relative to SMOW (*68*). As SC olivine is considered representative of Earth's mantle, bulk silicate Earth (BSE) also has a $\Delta^{17}O$ lower than SMOW by as much as ~ –0.1 ‰. During the analytical sessions for the two Ryugu samples at UCLA, analyses of SC olivine yielded $\delta^{18}O$ = 5.26 ±0.13 ‰ (1SD), $\delta^{17}O$ = 2.72 ±0.06 ‰, and $\Delta^{17}O$ = –0.065 ±0.005 ‰, respectively. Two analyses of air during this interval yielded $\delta^{18}O$ = 23.82 ±0.05 ‰ (1SD), $\delta^{17}O$ = 12.122 ±0.006 ‰, and $\Delta^{17}O$ = –0.265 ±0.032 ‰.

To compare our results to previous work, it is important to refer to a more accurate depiction of $\Delta^{17}O$ values relative to different oxygen reservoirs based on a mass fractionation relationship. This uses the logarithmic definitions of fractional deviations from standards, in which

$$\delta'^{18}O_{SMOW} = 10^3 \ln((^{18}O/^{16}O)_{Sample}/(^{18}O/^{16}O)_{SMOW}), \quad \text{(S5)}$$

and similarly for $\delta'^{17}O_{SMOW}$, and

$$\Delta'^{17}O = \delta'^{17}O_{SMOW} - \beta \times \delta'^{18}O_{SMOW} \quad \text{(S6)}$$

where β is mass-dependent fractionation coefficient. Mass-dependent fractionation then corresponds to β = 0.528 (*69, 70*). With these definitions for departures from the SMOW fractionation line, our SC olivine analyses obtained during the Ryugu analytical session give $\Delta'^{17}O$ = –0.104 ±0.006 ‰ and the value for air is –0.380 ±0.031 ‰. Both values are consistent with the previous work (*68*). The two A0107 Ryugu samples B and C have $\Delta'^{17}O$ values of 0.576 ±0.056 ‰ and 0.574 ±0.019 ‰ using this notation.

Methods at UG

An aliquot (1.42 mg) from Ryugu sample C0002 were analyzed along with two aliquots of the Orgueil CI chondrite (1.21 mg and 1.14 mg) and an aliquot of the Ivuna CI chondrite (0.92 mg) for comparison. The oxygen isotope composition was determined by infrared laser fluorination (*67*). Because of the potentially high reactivity of the Ryugu samples and potential of cross contamination, analyses were conducted using small, 2-pit sample holders that were transferred from an evacuated air lock into the fluorination chamber. The air lock was pumped down to ~5×10^{-6} mbar and heated using heating tape to ~100 °C for 24 h. The empty fluorination chamber was evacuated and heated to about 60 °C for 24 h before being exposed to ~ 50 – 100 mbar BrF_5 for ~ 15 min to remove any moisture sticking to the inner walls of the chamber. The amount of released O_2 (blank) was monitored by means of continuous flow mass spectrometry until it stabilized after ~ 7 fluorination steps at 0.01 to 0.02 µmol O_2.

After the air lock cooled to room temperature, sample holders (~5 × 10 × 8 mm) were introduced through a gate valve into the fluorination chamber. Samples were then exposed to BrF_5 (100–300 mbar) without laser heating for ~ 10 min to react the labile oxygen which was collected with the O_2 from laser-assisted fluorination. This procedure was used to collect oxygen from hydrous silicates that otherwise might be lost by prefluorination and to facilitate the successive laser heating step (reduce sputtering of sample material). Then, the sample was fluorinated by scanning the laser beam across the sample pit and successively increasing the laser energy up to 45 W. Despite the pre-fluorination, some sample material sputtered during the application of the laser.

After visible reaction ceased, sample O_2 gas was transferred via cold traps and an NaCl getter (for F_2 removal) to a 5 Å molecular sieve trap. From this trap, sample O_2 was transferred via a He gas stream (10 mL min^{-1}) through a 5 Å molecular sieve packed gas chromatography column (3 m, 1/8 inches, 50 °C) into a second 5 Å molecular sieve trap located connected to the Thermo 253 Plus mass spectrometer. After evacuation of He from this trap, sample O_2 was expanded at 50 °C into the bellows of the mass spectrometer.

Samples were measured relative to reference gas that was calibrated using O_2 released from SC olivine ($\delta^{18}O$ = 5.23 ‰, $\Delta'^{17}O$ = –0.052 ‰; see (*73*)). About 60 cycles (with 26 s integration time for sample and reference) were measured for each sample. During acquisition, sample and reference gas pressures were kept constant within ~ 1 %. For quality control, we ran SC olivine, CI chondrites Ivuna and Orgueil using the same technique. During this analytical session, air O_2 was measured (with complete separation of N_2 and partial separation of Ar; Ar could not be completely separated from O_2 at 50 °C). However, contamination of O_2 by Ar may lead to erroneously high $\Delta'^{17}O$; we measure $\Delta'^{17}O$ of –0.440 ‰, lower than the –0.432 ‰ value found in previous work (*68*). The timings of the entire fluorination, gas transfer and measurement procedure were controlled using LabVIEW software to avoid any user-specific effects. The sizes of the SC olivine and CI chondrite samples were adjusted to the amount of O_2 released from Ryugu, which corresponded to ~ 0.9 mg of SC olivine. The small samples sizes may have resulted in contamination by fluoro-organic components, leading to analytical uncertainties of ~ 0.5 ‰ for $\delta^{18}O$ and ~0.05 ‰ for $\Delta'^{17}O$ (2SD). The $\delta^{17}O$ and $\delta^{18}O$ data are reported relative to SMOW.

Electron Microscopy

Three polished sections (A0058-C1001, A0058-C2001 and C0002-C1001) were made from Ryugu samples A0058 and C0002, respectively. The Ryugu grains were individually embedded in 1-inch epoxy disks using the Buehler EpoxiCure 2 Resin. The sample disks were polished with an automatic polishing machine (Musashino Denshi MA-200e) at Hokkaido University. Diamond slurries with polycrystalline diamond particles of ~3 μm and then ~1 μm dissolved in ethylene glycol and polishing plates composed of copper and tin-antimony alloy were used for polishing. > 99.5 % ethanol was used for cleaning during and after the polishing. Polished sections of Ivuna were made by the same procedure. The polished sections were coated with a thin (~5 nm) gold film using a Leica EM ACE600 coater for backscattered electron (BSE) imaging and elemental analysis using an EDS detector.

BSE images were obtained with a field-emission scanning electron microscope (FE-SEM; JEOL JSM-7000F) at Hokkaido University. Quantitative X-ray elemental measurements were conducted with a 15 keV electron beam and an EDS detector (Oxford X-Max 150) installed on the FE-SEM. Beam currents of ~2 nA and ~1 nA were employed for the X-ray mapping and quantitative analysis, respectively. Mineral standards coated with a gold thin film (~5 nm) were used for standardization. BSE images and pseudo color images made by elemental mapping were used to determine petrologic and mineralogical characteristics of the samples (Fig. 1).

Secondary ion mass spectrometry (SIMS)

After electron microscopy was completed, the polished sections were recoated with an additional thin (~65 nm) gold film for SIMS measurements of oxygen and Mn-Cr isotope systematics.

The oxygen isotope compositions of dolomites and magnetite grains were measured with the Cameca ims-1280HR SIMS instrument at Hokkaido University with the analytical and instrumental settings same as previous work (*71*) as: A ~150 pA Cs^+ primary ion beam focused to ~5 μm was used. Primary and secondary acceleration voltages were set to +10 kV and –10 kV, respectively. We applied a 1 μm square raster to the primary beam during analyses to ensure a shallower depth of sputter crater, which suppresses changes in secondary ion intensity ratios during measurements. The typical ^{16}O count rates for dolomite and magnetite were ~1.7×10^8 counts per second (cps) and ~1.5×10^8 cps, respectively. The secondary $^{16}O^-$, $^{17}O^-$, and $^{18}O^-$ ions were measured simultaneously using the multicollection system consisting of a Faraday Cup (FC) (10^{11} Ω), an axial electron multiplier (EM), and a FC (10^{12} Ω), respectively. The mass resolving power (10 % valley) was set to ~6000 to resolve $^{17}O^-$ from $^{16}OH^-$. The data were collected for 30 cycles with 4 seconds integration time per cycle. The automatic centering program (dynamic transfer field aperture and magnetic field) was applied before data collection. The data were corrected for FC background and EM deadtime. The FC background was monitored during the presputtering of every measurement for ~30 s. Because the tail of the $^{16}OH^-$ peak overlaps the $^{17}O^-$ peak, we made a small tail correction (typically ~0.1 ‰, up to ~0.6 ‰) on $^{17}O^-$ based on $^{16}OH^-$ count rate measured at the end of each measurement.

The instrumental mass fractionation (IMF) for the O-isotope measurements of dolomite is sensitive to the iron contents (*72*). A series of dolomite-ankerite standards from University of Wisconsin-Madison (*72*) were used to calibrate the dependence of IMF on Fe# (=Fe/(Fe+Mg)). We measured 7 standards with different Fe# from 0 to ~0.8 and constructed a calibration curve using the fitting protocol with a Hill function (*72*). The $\delta^{18}O$ from the standards are normalized to those measured on the standard 6250 (Fe# = 0). The calibration curve we find is similar to previous results (*72*). We applied the IMF factor to each measurement of dolomites using the Fe# obtained in the electron microscopy measurements. The uncertainty of the calibration curve is less than 0.5 ‰.

The IMF for O-isotope measurements of magnetite was corrected using a polycrystalline magnetite standard from Chile (*73*). Due to possible crystallographic orientation effects (*74*), the IMF from magnetite grains varies more than the statistical uncertainties of the measurements. Because of this, we measured ~60 points from different crystals of the magnetite standard to determine the mean value and uncertainty (~2.1 ‰ in $\delta^{18}O$; 2 standard deviation, 2SD) involved in these measurements. The reported uncertainties in the O-isotope ratios were the larger of the external reproducibility of standard measurements (2SD) or internal precision (2 standard error, 2SE, of cycle data) of samples.

The ^{53}Mn-^{53}Cr isotope systematics of dolomite were measured with the ims-1280HR SIMS instrument at Hokkaido University. A ~100 pA $^{16}O^-$ primary beam focused to ~5 μm was used for data collection. Prior to the data collection, a ~1 nA beam was rastered over a 10×10 μm area for presputtering (250 s) to minimize the surface contamination of chromium. The secondary ions of $^{52}Cr^+$, $^{53}Cr^+$, and $^{55}Mn^+$ were measured simultaneously using three electron multipliers. The mass resolving power was ~6800, sufficient to resolve $^{53}Cr^+$ from interfering $^{52}CrH^+$. Isotope ratios were calculated using the total counts. Instrumental mass fractionation and Mn/Cr relative sensitivities were corrected using a synthetic calcite standard MACS-3NP (*75*). The relative sensitivity factor (RSF) of Mn/Cr may include a systematic error because of lack of suitable dolomite standards with identical matrix effects (*76*). The RSF values previously reported for dolomite are variable over ranges from 0.64 to 0.91 relative to the RSF of calcite

(*75-79*). This introduces uncertainties in the dating of the Ryugu samples. Therefore, we used the RSF of calcite, which is determined accurately with high precision and has been used to determine the ^{53}Mn-^{53}Cr isotope systematics of dolomite in previous studies (*34, 35*). The reported uncertainties (2SD) in chromium-isotope and ^{55}Mn/^{52}Cr ratios include both the internal precision of an individual analysis (2SE) and the external reproducibility (2SD). Linear regression models were fitted to the data using the IsoPlot model-1 software (*80*). The true age may lie over a range of 0.6 to 1.1 times the statistical value due to this uncertainty.

Thermogravimetric analysis coupled with mass spectrometry (TG-MS), and combination analyses of pyrolysis and combustion (EMIA-Step)

The A0040 Ryugu samples were used for TG-MS, and the A0040 and A0094 samples were used for EMIA-Step. The A0040 Ryugu (0.977 mg) and Ivuna (0.912 mg) samples were analyzed using a Thermo plus EVO2 TG-DTA8122 TG-MS Instruments at the Rigaku Co., Tokyo, Japan. Each sample of one or several chips was loaded into a Pt crucible and analyzed under a He flow of 200 ml min^{-1}. Mass loss from the samples was recorded as they were heated from 40 °C to 1000 °C at a rate of 20 °C min^{-1}. The uncertainty on the measured mass loss fraction is ~0.5 %. Evolved gases during TG were introduced into a quadrupole mass spectrometer without time loss to acquire a mass spectrum over the range m/z = 10–300 by electron ionization. Mass peaks of H_2O (m/z = 18) and CO_2 (m/z = 44) are calibrated to wt.% using calcium oxalate monohydrate $CaC_2O_4 \cdot H_2O$. The relative uncertainty due to this calibration is estimated to be 5 %.

Carbon and sulfur abundances were determined at the Horiba Techno Service Co., Ltd., Kyoto, Japan using a HORIBA EMIA-Step instrument for pyrolysis and combustion analyses. For carbon analysis, each sample of one or several chips was loaded into a quartz boat, covered with 60 mg of glass wool, and introduced into a quartz furnace at 800 °C with continuous flow of N_2 at a flow rate of 3.0 L min^{-1} (approximately 180 kPa). The sample was heated at 800 °C for 100 s. Then, the temperature of the heating element was increased linearly from 800 °C to 1000 °C at a rate of 1 °C s^{-1}, and held at 1000 °C for 250 s. The temperature change monitored at the sample position in the furnace was delayed relative to the programed heating profile due to the heat capacity of the furnace. The gas flow was then changed to O_2 at a rate of 3.0 L min^{-1} (approximately 180 kPa) at 450 s. The generated gases were sequentially transported into a copper oxide converter maintained at 600 °C with N_2 or O_2 flow and carbon species in the gas converted to CO_2. The gas flow containing CO_2 was dehydrated and the time variation of CO_2 intensity measured with a non-dispersive infrared (NDIR) detector. The NDIR signals were converted to carbon concentrations (wt.%) using a sodium hydrogen carbonate $NaHCO_3$ standard. The time sequence of the generated gases was controlled by kinetics of pyrolysis and combustion reactions of the sample under the experimental condition. The timing of CO_2 generations from carbonates, organic matter and graphite were calibrated using reference materials (Precipitated calcium carbonate CaCO3, purity >96%, particle size 12-15μm, The Association of Powder Process Industry and Engineering Japan, for carbonates; L-Tyrosine, purity>99.0%, Nacalai Tesque, Inc. for organic matter; Graphite, purity>99%, particle size 100-200 mesh, Rare Metallic Co., Ltd. For graphite) and their mixtures under the experimental condition. Therefore, the carbon present in different chemical forms in the sample is released at a different time, producing a time spectrum. The spectrum was deconvoluted into multiple peaks by fitting Voigt function models. Carbon concentration for each chemical state was determined by integrating fitted model.

For sulfur analysis, each sample of one or several chips was loaded into an alumina boat and introduced into a ceramic furnace under a continuous flow of O_2 at a rate of 3.0 L min^{-1} (approximately 180 kPa) maintained at 1450 °C at the sample position for 120 s. The generated gases including SO_2 gas were sequentially dehydrated and the time variation of the intensities was measured using the NDIR detector. The NDIR intensity is calibrated to sulfur concentration (wt.%) using a potassium sulfate K_2SO_4 standard. Integrated intensities with time correspond to the sulfur concentration in the sample.

The sample masses for carbon analyses were 0.91 mg (from A0040) for Ryugu and 0.80 mg for Ivuna; and for sulfur analyses, they were 0.89 mg (from A0040 and A0094) for Ryugu and 0.92 mg for Ivuna. The main source of uncertainty comes from the sample weighing that has a relative error of 10 % for samples of 1 mg.

Supplementary Text

Results

The chemical compositions of bulk Ryugu samples determined by XRF and ICP-MS are listed in Data S2. The elemental abundances, normalized to CI chondrite (*50*), are plotted in Figure 2. The representative composition for CM chondrites (*50*) is also plotted for comparison. High concentrations of tantalum for the Ryugu samples were observed, which reflect contamination from the Ta projectiles used in the sampling apparatus of Hayabusa2 that impacted the Ryugu surfaces (*11*). Trace elements compositions of a spare Ta projectile from the same lot as those used at Ryugu were determined by ICP-MS (Data S2). A mass-balance calculation shows that no other element was affected by the projectile contamination. Measurement uncertainty for individual data is smaller than the observed variations between independent measurements in most cases (Data S2). The observed variations are most likely due to heterogeneity at the small scales sampled and analyzed.

The isotopic ratio of $^{50}Ti/^{47}Ti$ and $^{54}Cr/^{52}Cr$ determined by MC-ICP-MS and TIMS are listed in Data S3 and plotted in Figure 3. The bulk Ti and Cr isotopic compositions of the Ryugu samples are similar to the CB (Bencubbin-like) and CI chondrite values in the CC meteorite region. However, the metal-rich nature of CB chondrites likely precludes their kinship with the Ryugu samples. The slightly lower $\varepsilon^{54}Cr$ values for Ryugu than CI chondrites could be due to heterogeneous distribution of isotopically anomalous carrier phases in Ryugu and CI chondrites. The presence of such phases in CI chondrite has previously been confirmed for Orgueil, which showed a large variation in $\varepsilon^{54}Cr$ values ranging from –8 to +90 (*81*).

The chromium isotope compositions and Mn/Cr ratios of dolomites in Ryugu and Ivuna are listed in Data S5. The data are plotted on ^{53}Mn-^{53}Cr isochron diagrams (Fig. 5). The slopes $(^{53}Mn/^{55}Mn)_0$ of isochron are regressed as $(2.55\pm0.35)\times10^{-6}$ with mean squared weighted deviation (MSWD) of 1.1 for Ryugu and $(3.14\pm0.28)\times10^{-6}$ with MSWD of 1.5 for Ivuna. The initial $\delta^{53}Cr_0$ is 12±29 for Ryugu and –41±51 for Ivuna.

The mass loss and differential thermogravimetry (DTG) curves for Ryugu and Ivuna determined by TG-MS are shown in Figure 6. Figure 6 also shows the mass-intensity curves generated during the measurements. The mass intensities were corrected by the blank run signals, and, therefore, they were generated from Ryugu and Ivuna. The mass spectra are

dominated by peaks at 18, 44, and 64 (Fig. S4). The peaks of m/z = 18 and 64 corresponded to H_2O generated from phyllosilicates and sulfates, and SO_2+S_2 generated from sulfates and sulfides, respectively. The SO_2+S_2 profile was much smaller in Ryugu than that in Ivuna, suggesting that abundance of sulfates is small in Ryugu because sulfides are abundant in the Ryugu sample (Fig. 1). Therefore, contribution of SO_2+S_2 to mass-loss is negligible for Ryugu, but not for Ivuna. The peaks at m/z = 44 corresponds to CO_2 generated from carbonates and organics. The CO_2 from organics was produced by oxidation of gases with the indigenous oxygen as well as with residual O_2 in the He flow atmosphere. The intensities are calibrated to concentrations in weight (Data S6).

The CO_2 curves generated from the Ryugu and Ivuna samples by EMIA-Step are shown in Figure 7. As in the TG-MS analysis, the first peak in the CO_2 curves is the result of decomposition of organics and the second peak is due to carbonate decomposition after which the CO_2 curves gradually decreased, suggesting progressive graphitization of organics and loss of labile functional group. The graphitized organics was completely combusted at ~500 s. The CO_2 curve was deconvoluted into multiple peaks by fitting Voigt models. The peak at 140 s corresponds to CO_2 generated from carbonates, i.e., inorganic carbon peak, and the other peaks corresponded to carbon species generated from organics, i.e., organic carbon peaks. The area of each peak corresponds to the carbon concentration for a chemical state of carbon in the samples (Data S6). The total sulfur contents of Ryugu and Ivuna were also determined (Data S6). Using the organic carbon contents coupled with the composition of insoluble organic matter (IOM) in CI chondrites (*82*), we calculated the organic hydrogen contents in the sample. The total hydrogen contents were calculated from the organic hydrogen contents and the H_2O contents obtained by the TG-MS. Recommended values of inorganic hydrogen, total hydrogen, inorganic carbon, organic carbon, and total carbon for the Ryugu and Ivuna samples are summarized in Data S6.

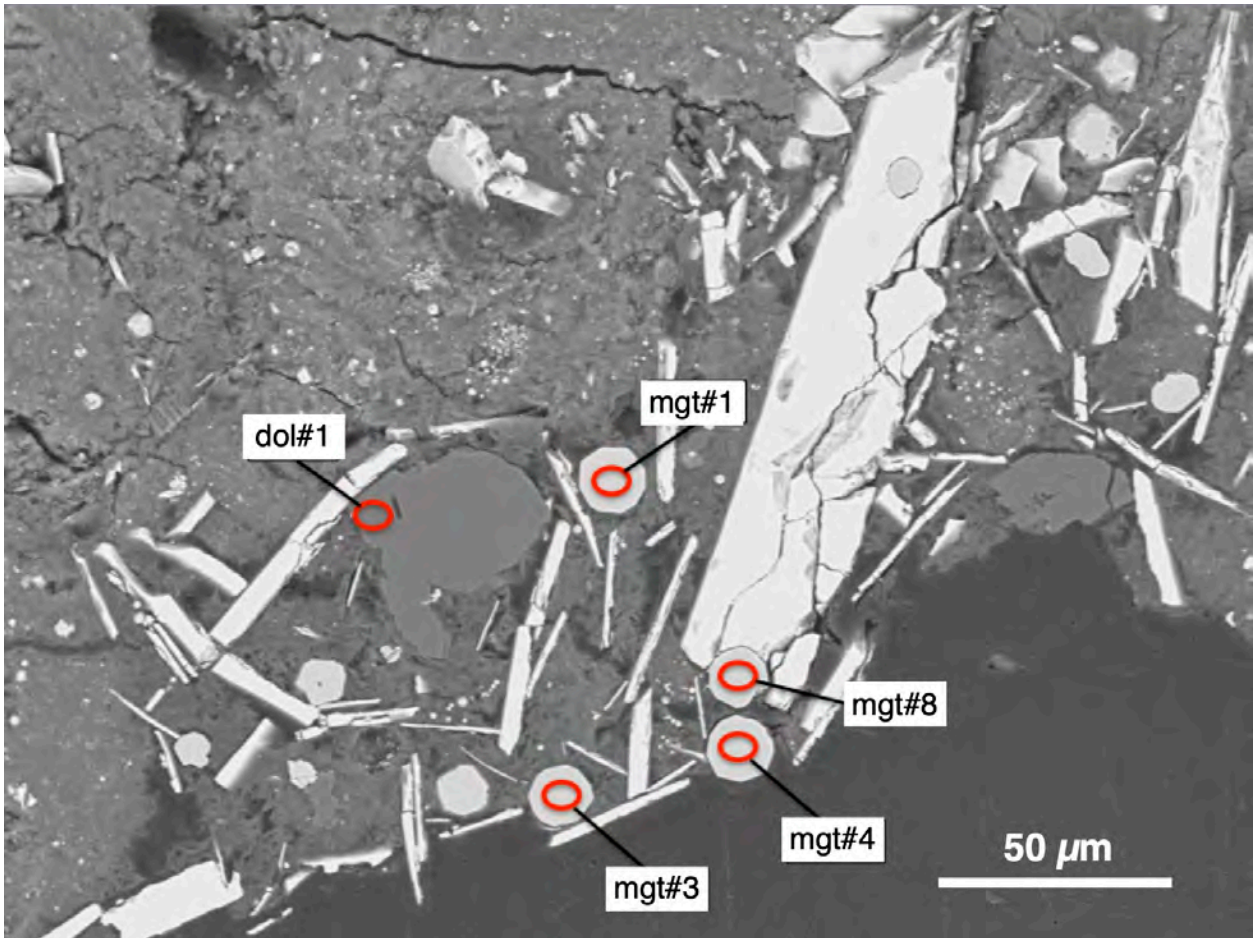

Fig. S1. Measurement position of oxygen isotopes for a dolomite equilibrated with magnetites in Ryugu sample A0058-C1001. dol: dolomite, mgt: magnetite with measurement # in Data S4. The resulting measurements are shown in Fig. 4.

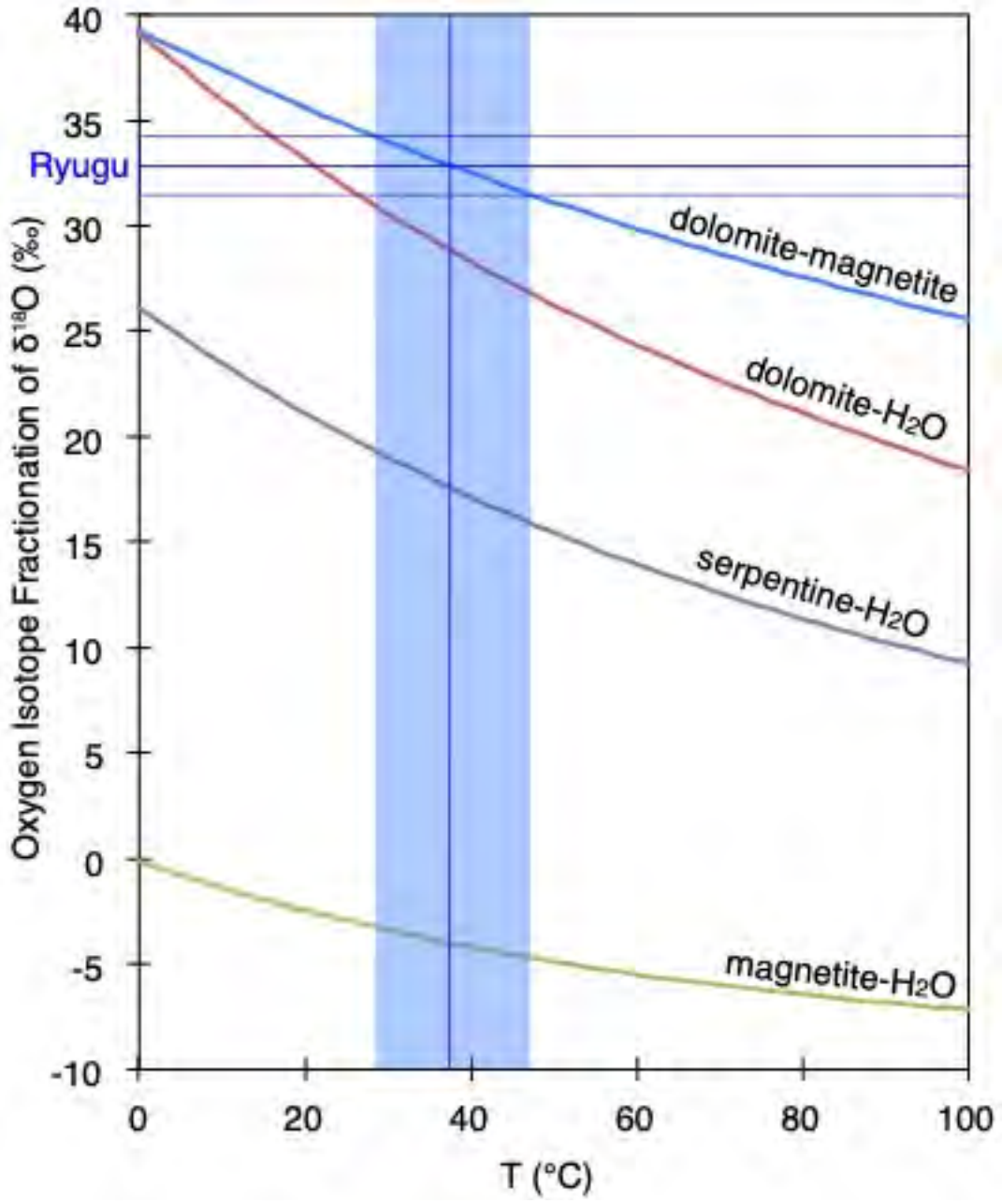

Fig. S2. Oxygen isotope fractionation of $\delta^{18}O$ for dolomite-magnetite, dolomite-H_2O, magnetite-H_2O, and serpentine-H_2O as a function of temperature. Each curve corresponds to the mineral pair or mineral-H_2O pair shown in the figure. The curves used were from previous works (*27-30*). The oxygen isotope fractionation of the Ryugu sample is indicated as horizontal blue line with uncertainty. The shaded region is temperature range corresponding to the fractionation, suggesting dolomite-magnetite coprecipitation occurred at 37 ±10 °C.

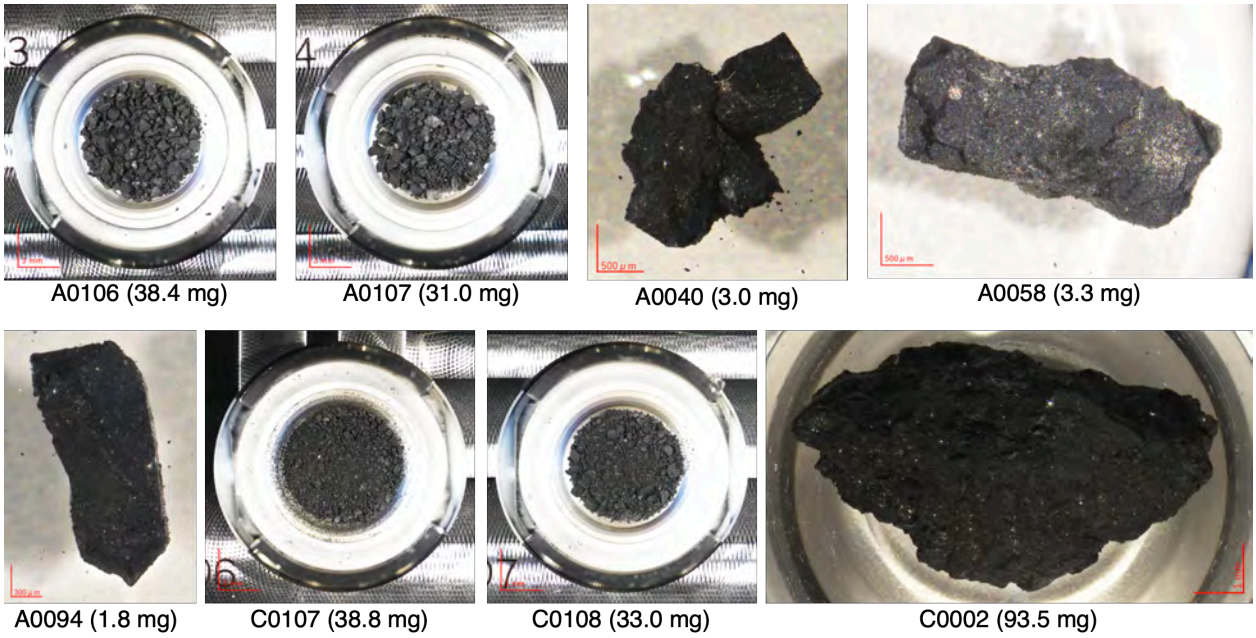

Fig. S3. Opitical images of allocated samples. Whole quantities for A0107, A0040, A0058, A0094, C0108 are allocated, whereas 15.7 mg for A0106, 12.9 mg for C0107 and 28.8 mg for C0002 are allocated.

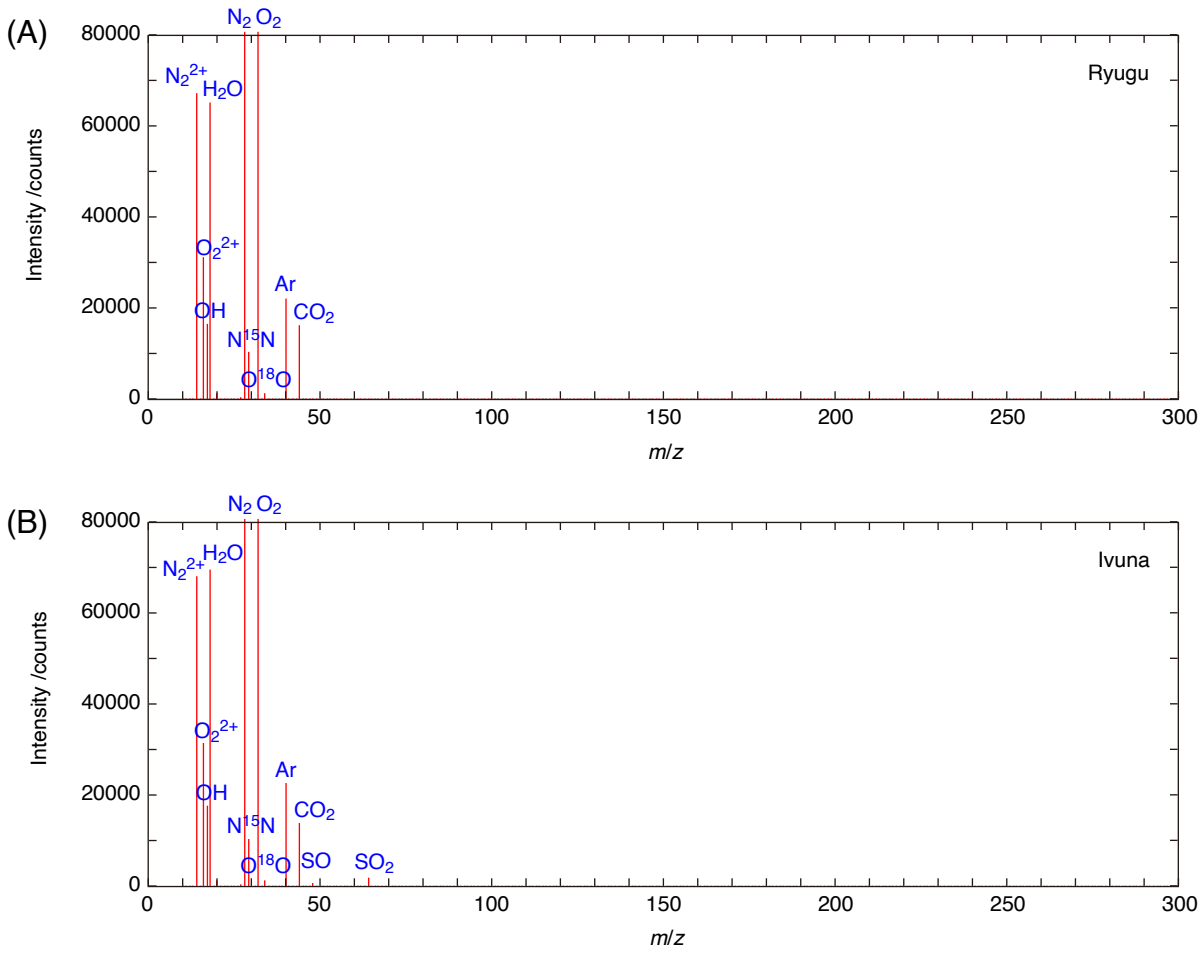

Fig. S4. Mass spectrum of released gas during TG-MS analyses. (A) Ryugu. **(B)** Ivuna. m/z = 10–300 are measured. Major signals are assigned as molecules in figures. Signals of N_2^{2+}, O_2^{2+}, N_2^{+}, O_2^{+}, $O^{18}O^{+}$, and Ar^{+} are due to minor Air contamination into the He flow during measurements. A small peak of m/z = 27 may be HCN^{+}.

Supplementary Data are provided by excel files (.xlsx).

Caption for Data S1. (separate .xlsx **file)**
Conditions for ICP-QMS operation.

Caption for Data S2. (separate .xlsx **file)**
Chemical composition (μg/g) of Ryugu samples.

Caption for Data S3. (separate .xlsx **file)**
Isotopic ratios for Ti and Cr of Ryugu samples and meteorites.

Caption for Data S4. (separate .xlsx **file)**
Oxygen isotopic composition (‰) of Ryugu, Ivuna and Orgueil.

Caption for Data S5. (separate .xlsx **file)**
Manganese-chromium isotope data of dolomites from Ryugu and Ivuna.

Caption for Data S6. (separate .xlsx **file)**
Hydrogen, carbon, and sulfur concentrations of Ryugu and Ivuna determined by TG-MS and EMIA-Step.

Caption for Data S7. (separate .xlsx **file)**
Thermogravimetric analysis coupled with mass spectrometry (TG-MS) for Ryugu and Ivuna.

Caption for Data S8. (separate .xlsx **file)**
Carbon concentration curves (wt. %) released from Ryugu and Ivuna by combination analyses of pyrolysis and combustion (EMIA-Step).

Caption for Data S9. (separate .xlsx **file)**
Standards used for XRF analyses using Rigaku ZSX Primus IV.